

Key Points:

- Rotating convection in Europa's ocean drives a net torque on the ice shell through turbulent drag at the ice-ocean interface
- The ice-ocean torque spins up the ice shell if the convective forcing is weak, and spins down the shell if the forcing is strong
- Nonsynchronous rotation of Europa's ice shell may be controlled by the dynamics of the underlying ocean

Supporting Information:

Supporting Information may be found in the online version of this article.

Correspondence to:

H. C. F. C. Hay,
hamish.hay@earth.ox.ac.uk

Citation:

Hay, H. C. F. C., Fenty, I., Pappalardo, R. T., & Nakayama, Y. (2023). Turbulent drag at the ice-ocean interface of Europa in simulations of rotating convection: Implications for nonsynchronous rotation of the ice shell. *Journal of Geophysical Research: Planets*, 128, e2022JE007648. <https://doi.org/10.1029/2022JE007648>

Received 31 OCT 2022

Accepted 14 FEB 2023

Corrected 29 MAR 2023 and 14 JUN 2023

This article was corrected on 29 MAR 2023 and 14 JUN 2023. See the end of the full text for details.

© 2023 Jet Propulsion Laboratory, California Institute of Technology. Government sponsorship acknowledged. This is an open access article under the terms of the [Creative Commons Attribution-NonCommercial License](#), which permits use, distribution and reproduction in any medium, provided the original work is properly cited and is not used for commercial purposes.

Turbulent Drag at the Ice-Ocean Interface of Europa in Simulations of Rotating Convection: Implications for Nonsynchronous Rotation of the Ice Shell

H. C. F. C. Hay^{1,2}, I. Fenty¹, R. T. Pappalardo¹, and Y. Nakayama³

¹Jet Propulsion Laboratory, California Institute of Technology, Pasadena, CA, USA, ²Department of Earth Sciences, University of Oxford, Oxford, UK, ³Institute of Low-Temperature Science, Hokkaido University, Sapporo, Japan

Abstract Europa's geologically scarred surface shows significant evidence that the ice shell may have rotated nonsynchronously in the past. The long-term spin state of the ice shell is controlled by the time-mean torques acting upon it. A torque that has not been previously considered is exerted due to drag from oceanic currents beneath the ice. We estimate this torque for the first time by performing global, nonhydrostatic, three-dimensional simulations of Europa's ocean, including nonlinear turbulent boundary layer drag at the seafloor and ice-ocean interface. Our simulations show that ocean dynamics, which manifest in alternating east-west jets, result in a net torque on the ice shell. The torque can act to either spin up or spin down the ice shell depending on the strength of convection, suggesting that a torque reversal can occur as Europa's interior thermally evolves. Scaling analysis indicates that an average jet speed of at least $\sim 1 \text{ cm s}^{-1}$ is required for the ice-ocean torque to be comparable to the tidal torque acting to spin up the ice shell. Our results suggest that ocean currents may contribute to any nonsynchronous rotation of the ice shell. Consequently, Europa's present-day spin state may hold information about the dynamics of its subsurface ocean.

Plain Language Summary Europa's subsurface ocean is heated from below via tidal heating and radioactive decay of the rocky interior, while being cooled from above by its frozen surface. Simulations and laboratory experiments suggest that this results in convection, whereby heat is transported in rising and sinking plumes of warm and cold water. These plumes are influenced by Europa's rotation and consequently form jets of alternating east-west oceanic currents. At the surface, the flowing ocean exerts friction on the ice, causing it to move. We simulate this process using a large-scale computer model of Europa's ocean. Our simulations show that the jets can exert enough friction on the ice to be relevant in understanding how the ice shell rotates. We suggest that this may have increased or decreased Europa's spin rate in the past. Because of this effect, precise measurements of how fast Europa's surface is spinning may hold clues about how the ocean inside is flowing around today.

1. Introduction

Convection is thought to be the dominant mode of heat transfer in the liquid interiors of Europa and other ocean-bearing icy moons (e.g., Bire et al., 2022; Kverka & Čadež, 2022; Soderlund, 2019; Soderlund et al., 2014). Convective plumes rising from the seafloor and sinking from the frozen ocean surface are likely influenced by the rotation of these bodies (Bire et al., 2022; Soderlund, 2019). An ubiquitous feature of numerical and laboratory experiments of rotating convection is the formation of time-mean zonal jets that form cylinders aligned with the rotation axis (e.g., Aurnou et al., 2007; Cheng et al., 2018; Christensen, 2002; Gastine et al., 2016; Kaspi et al., 2009; Soderlund, 2019; Soderlund et al., 2013). These jets, which can flow eastward or westward depending on the moon's rotation rate, strength of basal heating, and their distance from the rotation axis, must locally impart momentum into the seafloor and ice shell as the ocean turbulently interacts with these boundaries. However, drag, the process that fluxes momentum into the ice, has not been studied in detail in these numerical models primarily due to the overly large viscosity required in global circulation models. The present manuscript addresses this.

On Earth, the atmosphere, ocean, and outer core constantly flux angular momentum to and from the solid Earth via changes in the strength of circulation and fluid's mass distribution (Barnes et al., 1983; Munk & Groves, 1952; Munk & MacDonald, 1960; Wahr, 1983; Wahr et al., 1981). This is observable through changes in Earth's length of day (LOD) and wobble of its rotation pole (e.g., Chao, 1989; Rosen & Salstein, 1983). The atmosphere is

generally thought to be the dominant, nontidal contributor to Earth's LOD changes, which are on the order of 0.1–1 ms (Lambeck, 1980). While Europa does not have a significant atmosphere, its ice shell's moment of inertia (MoI), the rotational analogue of mass that acts to resist changes in rotation, is far smaller than Earth's mantle. For a thin spherical ice shell of density ρ_i and thickness h_i at Europa's mean radius R_e , Earth's mantle's MoI is roughly $M_m R_m^2 / 10 R_e^4 h_i \rho_i \sim 10^5$ times greater than Europa's ice shell's, where M_m and R_m are the mantle's mass and radius, respectively. A given exchange of angular momentum between the ocean and ice shell will consequently result in far bigger changes in Europa's surface rotation rate than for the solid Earth, at least in the absence of other torques.

Europa's rotation rate is thought to be near-synchronous, such that one European day is equivalent to the time taken to orbit Jupiter. Yoder (1979) for Io, and later Greenberg and Weidenschilling (1984) for Europa, point out that perfectly synchronous rotation results in a net tidal torque on the satellite due to its eccentric orbit. This implies that the ice shell would be constantly spinning up. A slightly faster-than-synchronous rotation rate is required for the orbit-mean tidal torque to become zero and therefore for Europa's rotation rate to be in equilibrium. Ojakangas and Stevenson (1989) additionally find that thickness variations in the ice shell due to tidal heating permit a slow nonsynchronous rotation. This is because any mass asymmetry due to tidal heating will only cancel out the tidal torque that spins up the satellite when the ice shell is in thermal disequilibrium (i.e., misaligned with the Jupiter), promoting a constant state of dynamic equilibrium. However, if nonsynchronous rotation is present at Europa, the current period of full rotation relative to synchronous is constrained to be greater than 10,000 years based on the observed position of surface features between the Voyager 2 and Galileo spacecraft encounters (Hoppa et al., 1999). There are also theoretical arguments against nonsynchronous rotation, including torques induced by permanent mass asymmetry (Bills et al., 2009; Greenberg & Weidenschilling, 1984) and elasticity of the ice shell (Goldreich & Mitchell, 2010). Yet, a large number of tectonic features on the surface can be explained most easily by the presence of nonsynchronous rotation (Geissler et al., 1998; Hurford et al., 2007; Jara-Oru  & Vermeersen, 2011; Kattenhorn, 2002; McEwen, 1986; Rhoden & Hurford, 2013; Rhoden et al., 2010; Selvans, 2009; Spaun, 2002) and have also been suggested for Enceladus (Patthoff et al., 2019). Dynamical modeling suggests that the hemispherical impact crater distribution should be heavily asymmetrical, but this is not the case, implying some amount of nonsynchronous rotation for both Europa and Ganymede (Zahnle et al., 1998, 2001, 2003, 2008). Furthermore, several of these lines of evidence suggest that any nonsynchronous rotation may occur at discrete periods in time, thereby requiring some mechanism to stop and start (e.g., McEwen, 1986). Ultimately, Europa's long-term rotation rate, Ω , depends on both its MoI, I , and the sum of all time-mean torques, \mathcal{T} , that act upon it (Lambeck, 1980). The purpose of this study is to add to the current understanding of what may govern Europa's rotation rate over time by considering the torque that is a natural result of convection in the ocean.

Our manuscript is organized as follows. In Section 2, we describe rotating convection, the nondimensional parameters that control the problem and our suite of numerical simulations of convection in Europa's subsurface ocean. We analyze the resulting dynamics at the near surface with focus on the time-mean and turbulent velocity field. In Section 3, we calculate the resulting stresses and associated net torque from our numerical model. We determine the properties of the ocean dynamics that lead to the calculated torque and use this to derive rough estimates of the ice-ocean torque that is applicable over a wider parameter space than simulated. Finally, we argue in Section 4 that this torque can in some cases be similar in magnitude to Europa's tidal torque and consequently may play a role in the rotation of the ice shell.

2. Theory and Numerical Convection Modeling

2.1. Rotating Convection and the Tangent Cylinder

Rotation prevents convective plumes from freely rising through the ocean. In quasi-linear convection, this can, roughly speaking, be attributed to Coriolis forces deflecting a plume's ascent from a simple radial trajectory away from the seafloor to follow a path strongly aligned with the rotation axis. The depth that these plumes rise through is then no longer just the ocean thickness, D , but the column thickness given by following lines parallel to the rotation axis, D_c , illustrated in Figure 1. This is a strong function of latitude, and importantly, features a discontinuity at the equatorial seafloor where the column thickness abruptly doubles (Heimpel & Aurnou, 2007). The discontinuity's location is often described by an imaginary bounding surface that is tangent to the seafloor at the equator, known as the tangent cylinder (Figure 1). In the most rotationally constrained systems, where buoyancy forcing is relatively weak, the tangent cylinder plays a huge role in the resulting dynamics. Convection can be severely restrained within the tangent cylinder, where rotational effects are most prominent, limiting the effi-

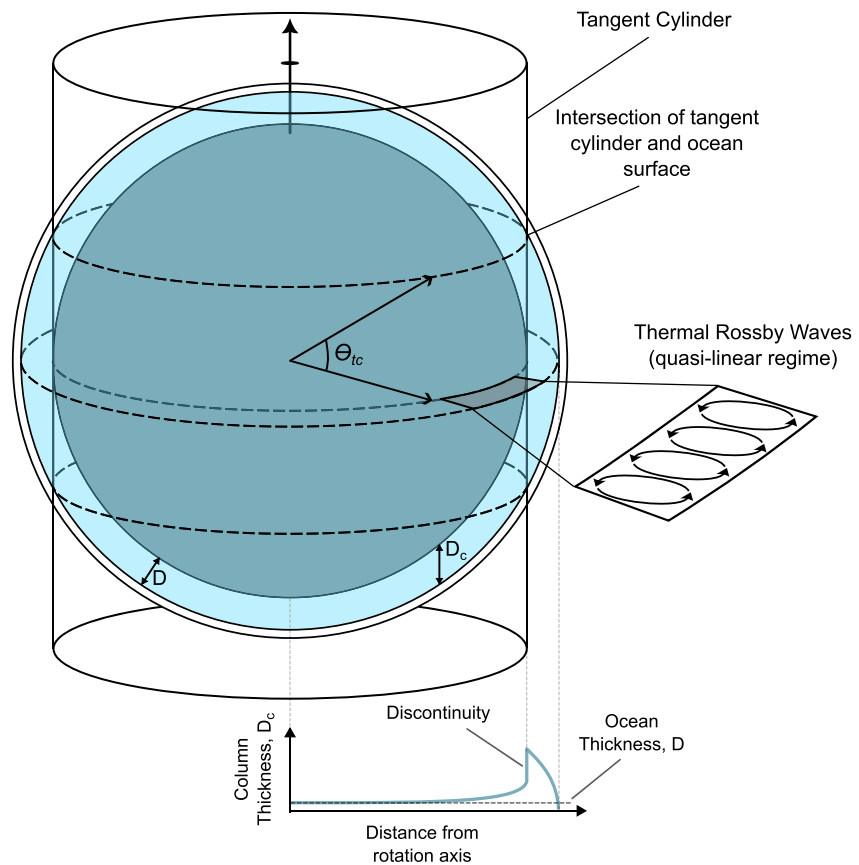


Figure 1. Illustration of the problem and the tangent cylinder. An ocean of uniform thickness, H , lies between two solid surfaces. When ocean dynamics are constrained by rotation, the relevant thickness becomes the column thickness parallel to the axis of rotation. This features a sharp discontinuity at the equatorial seafloor. Thermal Rossby waves are illustrated on the right, which lead to equatorial superrotation in the case of quasi-linear rotating convection.

ciency of convective heat transfer. Outside the tangent cylinder, convection takes on a different form—sometimes intuitively described as equatorial “rolls,” but more technically *thermal Rossby waves*. These waves tilt in the direction of planetary rotation due to the curvature of the spherical ice shell in order to conserve potential vorticity, transporting angular momentum outward as they do (Busse, 2002). Equatorial superrotation, a common feature of simulations of rotating convection, is driven by this eddy flux of prograde angular momentum (Kaspi et al., 2009).

When buoyancy forcing is stronger, plumes rise sufficiently quickly that they are influenced by rotation in a different way. At the equator, plumes rising away from the rotation axis rapidly deflect toward the west in order to conserve angular momentum, $M_{eq} = \Omega r^2 + ur$, where r is the radius and u is the fluid's zonal velocity. This drives low-latitude retrograde rotation with corresponding high-latitude prograde jets that are required to conserve global angular momentum. There is therefore a net flux of prograde angular momentum from low to high latitudes. This behavior is seen in the ice giants, Uranus and Neptune (Aurnou et al., 2007; Soderlund et al., 2013). As we will see, the two types of rotating convection outlined above manifest in our numerical results depending on the nondimensional parameters set in the model.

2.2. Nondimensional Parameters

Numerous studies have attempted to simulate convection in the subsurface oceans of icy moons (Amit et al., 2020; Ashkenazy & Tziperman, 2021; Bire et al., 2022; Goodman & Lenferink, 2012; Goodman et al., 2004; Kvorka & Čadež, 2022; Soderlund, 2019; Soderlund et al., 2014). An inherent difficulty in simulating such systems, especially at global scales, is the inability of current computing power to resolve turbulence. This problem can be circumvented by using artificially high fluid viscosities to filter out the smallest length scales of turbulence

Table 1
European Constants Used in the Numerical Simulations

Parameter	Symbol	Value
Radius	R	1,561 km
Rotation period	P	306,000 s
Surface gravity	g	1.3 m s^{-2}
Ocean thickness	D	100 km
Specific heat capacity	c_p	$4,000 \text{ J kg}^{-1} \text{ K}^{-1}$
Coefficient of thermal expansion	α	$2 \times 10^{-4} \text{ K}^{-1}$
Diffusivity	κ	$61.6 \text{ m}^2 \text{ s}^{-1}$
Viscosity	ν	$61.6 \text{ m}^2 \text{ s}^{-1}$
Ocean density	ρ_o	$1,000 \text{ kg m}^{-3}$
Top/bottom drag coefficient	c_D	0.002

such that the remaining dynamics can be resolved on the numerical grid. The fluid then requires a greater buoyancy forcing (e.g., geothermal heat flux) in order to overcome enhanced viscous forces to allow for convection. The dynamics of the “real” solution can then be estimated by rescaling the solution into the correct parameter space. Soderlund (2019) outlines this method, which utilizes existing scaling laws relating key nondimensional parameters defining the properties of the ocean to the fundamental parts of the resulting oceanic behavior. The three main nondimensional parameters controlling the convective behavior of the ocean are the Rayleigh, Ekman, and Prandtl numbers, respectively,

$$\text{Ra} \equiv \frac{\alpha g \Delta T D^3}{\nu \kappa}, \quad \text{Ek} \equiv \frac{\nu}{\Omega D^2}, \quad \text{Pr} \equiv \frac{\nu}{\kappa}, \quad (1)$$

where α is the ocean's coefficient of thermal expansion, g is gravity that we assume does not vary with depth, D is the ocean's thickness, Ω is Europa's rotation rate, ΔT is the vertical superadiabatic temperature contrast across the ocean, ν is the kinematic viscosity, and κ is the thermal diffusivity. Values of these constants used in our Europa simulations are given in Table 1.

The Rayleigh number indicates the ratio of buoyancy and thermal diffusivities so can be related to the geothermal and tidal heating rate. Ra in all of our simulations exceeds the critical Rayleigh number required for convection. The Ekman number indicates the relative role of rotation versus viscous forces. For icy satellite interiors, Ek is thought to be 10^{-10} to 10^{-12} (Soderlund, 2019; Soderlund et al., 2014). The Prandtl number indicates the relative role of viscous to thermal diffusion. Pr is expected to be about 10 for icy ocean worlds, though following Soderlund et al. (2014), Soderlund (2019), we assume $\text{Pr} = 1$ as it is more computationally feasible.

2.3. Numerical Model

We simulate Europa's subsurface ocean using the MITgcm, a general circulation model designed to simulate oceanic flow across many length scales (Marshall et al., 1997). The model solves the dimensional, nonhydrostatic primitive equations under the Boussinesq assumption using a finite volume discretization. The full, three-dimensional Coriolis force is retained. The ocean's linear equation of state depends only on the potential temperature of the ocean. The seafloor is rigid while the ocean surface is treated as a deformable free surface. Salinity and the mechanical and gravitational effects of the ice shell are neglected for simplicity (e.g., Beuthe, 2016; Lobo et al., 2021; Matsuyama et al., 2018; Zhu et al., 2017). The global domain is discretized over a cubed-sphere grid (Ronchi et al., 1996) with an average horizontal resolution of 3.4 km. The 100-km-thick ocean is split into 58 vertical levels, moving from a control volume thickness of 500 m at the boundaries to 2 km in the ocean interior. Each of the six cubed-sphere faces is split into 510×510 , leading to over 90.5 million finite volumes over which the fundamental equations are discretized ($6 \times 58 \times 510^2$). Each simulation is run in parallel across 256 cores on the NASA Pleiades high-performance supercomputing cluster.

Our setup is intentionally similar to Soderlund (2019) with the main differences being the numerical discretization and how the boundary conditions are implemented. To drive convection, the ocean is forced with a superadiabatic temperature differential, ΔT , from bottom to top. This is implemented in the MITgcm by forcing the top and bottom volumes toward the desired temperature over some timescales. We choose a timescale that is twice the model's time step, which in effect yields constant temperatures at the model top and bottom. We note that in the MITgcm's finite volume discretization, temperature is defined as a volume-averaged quantity. This means that the volume-averaged temperature across the entire top and bottom cell volumes is set to a single temperature. A small, random, spatially varying temperature perturbation on the order of $10^{-3} \Delta T$ is applied to the initial conditions to initiate convection. The superadiabatic temperature differential values are chosen utilizing Rayleigh–Nusselt number (Ra–Nu) scaling laws following Soderlund (2019), giving a range of Rayleigh numbers from 6.67×10^5 to 6.67×10^7 (Table 2). Specifically, we use the nonrotating diffusivity-free scaling from Gastine et al. (2015), $\text{Nu} = 0.07 \text{Ra}^{1/3}$, and the rapidly rotating scaling from Gastine et al. (2016), $0.15 \text{Ra}^{3/2} \text{Ek}^2$. With a fixed Ekman number of $3\text{e}-4$, we expect these Ra to broadly span a range of potential Europas that experience minimal heating at the seafloor due to only radiogenic decay to the extreme scenario where Europa's silicate

Table 2
Rayleigh Numbers of the Simulations Suite

Rayleigh number	ΔT
6.67×10^5	9.73×10^{-3}
9.80×10^5	1.43×10^{-2}
1.43×10^6	2.09×10^{-2}
2.10×10^6	3.07×10^{-2}
3.09×10^6	4.51×10^{-2}
4.54×10^6	6.63×10^{-2}
6.67×10^6	9.73×10^{-2}
9.80×10^6	1.43×10^{-1}
1.43×10^7	2.09×10^{-1}
2.10×10^7	3.07×10^{-1}
3.09×10^7	4.51×10^{-1}
4.54×10^7	6.63×10^{-1}
6.67×10^7	9.73×10^{-1}

Note. The Ekman and Prandtl numbers are fixed to $Ek = 3e - 4$ and $Pr = 1$, respectively.

interior is as efficient at dissipating tidal energy as Io (O'Brien et al., 2002). All other model parameters are given in Table 1. The models are run to a state of statistical convergence, identified using their global-mean kinetic energy field.

2.4. Boundary Layer Drag

In reality, our numerical models cannot resolve the mechanical boundary layers that must be present at the ice-ocean interface and seafloor that result in the transfer of momentum between solid and fluid. To circumvent this, we apply a drag stress at the ocean top and bottom that scales quadratically with the near-boundary velocity, an approach common to terrestrial studies involving barotropic tides (e.g., Jayne & St. Laurent, 2001) and ice-ocean interaction (Goosse & Fichefet, 1999; Lu et al., 2011; Steele et al., 1989). Assuming the ice shell and seafloor are stationary in the rotating frame and neglecting any large topographic variations at these interfaces, the turbulent drag stress tangential to the boundary experienced by a moving water parcel is (e.g., Goosse & Fichefet, 1999),

$$\tau_h = \rho_o c_D |\mathbf{u}_h| \mathbf{u}_h, \quad (2)$$

where c_D is a nondimensional drag coefficient and the velocity $\mathbf{u}_h \equiv (u e_\phi, v e_\theta)$ and stress $\tau_h \equiv (\tau_\phi e_\phi, \tau_\theta e_\theta)$ vectors are tangential to the surface, where e_θ and e_ϕ are the latitude and longitude unit vectors defined in Appendix A. As we ignore topography at the seafloor and ice-ocean interface, Equation 2 only accounts for turbulent drag due to skin friction. It therefore represents a minimum estimate for the ice-ocean drag for a given velocity field.

Quadratic bottom/top drag has been applied in numerical studies of tidal dissipation in icy satellite oceans (Chen et al., 2014; Downey et al., 2020; Hay & Matsuyama, 2017, 2019; Vincent et al., 2022), but we are the first to present it in simulations of ocean convection. Most studies use either stress-free (Soderlund, 2019; Soderlund et al., 2014) or no-slip boundary conditions (Amit et al., 2020; Ashkenazy & Tziperman, 2021; Bire et al., 2022). Zeng and Jansen (2021) use a linear drag, but only at the seafloor. Kvorka and Čadež (2022) explore the differences between stress-free and no-slip boundary conditions in numerical simulations of convective heat transfer in Titan's ocean, and they show that it can have a strong impact on the distribution of surface convective heat fluxes. Studies that do neglect drag (free-slip) do so because the artificially high viscosity used in the numerical model can cause the viscous boundary layer to play an overly large role in altering the interior dynamics (King et al., 2009). Importantly, the fluid viscosity does not appear in our expression for drag (Equation 2). This means that in our simulations the role of viscosity is not exaggerated, at least at the ocean's boundaries. We can show this by taking the ratio of the bottom/top drag stress in Equation 2 with the stress associated with the no-slip boundary condition. To order of magnitude, the ratio is,

$$\frac{\rho_o c_D |\mathbf{u}_h|}{\rho_o \nu \frac{\partial u}{\partial z}} \sim \frac{\rho_o c_D U^2}{\rho_o \nu U / \Delta z} = \frac{c_D U \Delta z}{\nu}, \quad (3)$$

which is about 0.01 for a characteristic velocity of $U = 1 \text{ m s}^{-1}$, which is typical of our most energetic simulations (Figure 3), a vertical grid spacing of $\Delta z = 250 \text{ m}$ at the top/bottom of the domain, $c_D = 0.002$, and $\nu = 61.6 \text{ m}^2 \text{ s}^{-1}$ as used in our simulations (Table 1). Our simulations therefore have a boundary stress that is at least two orders of magnitude smaller than that associated with the no-slip boundary condition. The simulations would require a near-boundary characteristic velocity of order 100 m s^{-1} for the two sources of boundary stress to become equal in our particular setup or a much coarser vertical resolution at the boundary. We note that our study is not the first to replace the no-slip condition with stress due to bottom/top drag (e.g., Deremble et al., 2011).

While the drag in Equation 2 is independent of viscosity, it does depend on the empirical drag coefficient, c_D . In terrestrial tidal literature, $c_D = 0.002$ – 0.003 (e.g., Egbert & Ray, 2001) though a Europa-appropriate value depends on the roughness length scale of the solid surface. Barotropic tidal dissipation studies on Europa and other icy moons use either $c_D = 0.002$ for bottom drag (Chen et al., 2014; Hay & Matsuyama, 2017) or a value

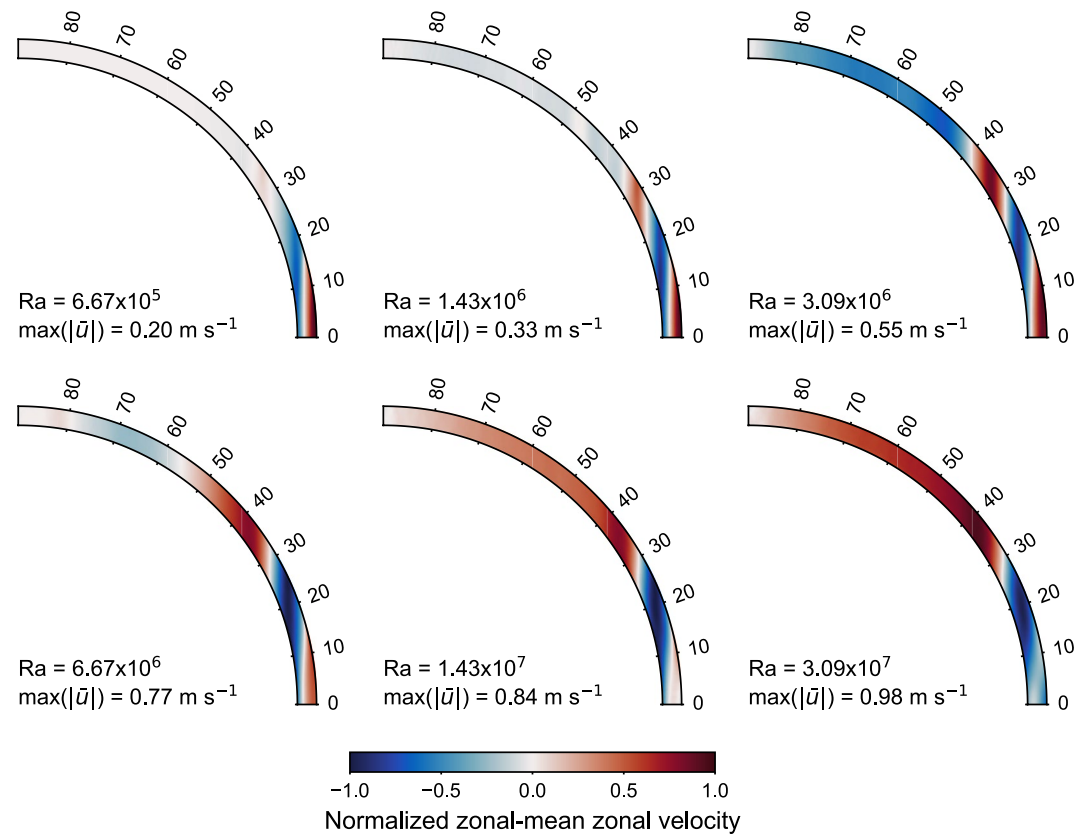


Figure 2. Meridional (north–south) slices of the time- and zonal-mean zonal velocity field for different Rayleigh numbers, Ra , increasing from top left to bottom right. The zonal velocity field is symmetric about the equator, so only the northern hemisphere is shown. The color bar is normalized with the maximum absolute flow speed given in the corner of each plot.

twice that to account for the addition of top drag (Hay & Matsuyama, 2019; Tyler, 2011). Lu et al. (2011) summarize a range of estimates for c_D at the base of sea ice in their Table 1, where it usually falls between 0.001 and 0.01. There is no reason to suggest that Europa's drag coefficient will fall outside these values at present. We use $c_D = 0.002$ at both top and bottom boundaries for best comparison to these previous studies and assume that it is spatially constant. Our choice of drag law is further discussed in Section 4.6.1.

2.5. The Oceanic Velocity Field

Our simulations, like others, are dominated by alternating, axes symmetric, zonal (east-west) jets, shown in the zonal-mean meridional (north-south) slices in Figure 2. We find a superrotating equatorial jet with one to two alternating jets at higher latitudes for the lowest Ra simulations. As Ra increases, higher latitudes also begin to develop zonal-mean jets. The equatorial jet switches sign to become retrograde in the highest Ra simulations, which is accompanied by strong prograde flow in the midlatitudes to high latitudes. This changing behavior as a function of Rayleigh number is broadly consistent with that outlined in Section 2.1. In the quasi-linear regime (low Ra), the dominant mean zonal flows are restricted to outside the tangent cylinder and are prograde at the equator, whereas with highly nonlinear convection (high Ra), retrograde flows exist at low latitudes.

The evolution of the zonal-mean zonal velocity field as a function of Ra is perhaps best shown at the surface, given in Figure 3. Again, the two most striking characteristics of the surface mean flow are the reversal of the low-latitude jets and development of fast high-latitude prograde flow for the highest Rayleigh numbers simulated. The intersection of the tangent cylinder at the surface occurs at a latitude $\theta_{tc} = \cos^{-1}(1 - D/R) \sim 20^\circ$ for our assumed ocean thickness of $D = 100$ km. Figure 3 shows that most superrotation is bounded to occur outside of the tangent cylinder when $Ra \lesssim 10^7$. High Ra retrograde rotation, while bounded to low latitudes, extends both outside and within the tangent cylinder.

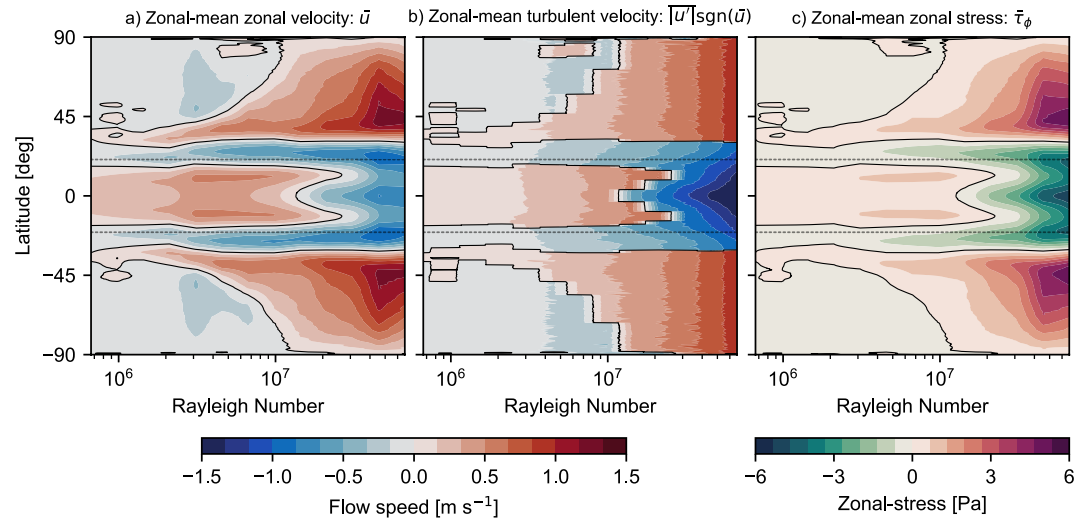


Figure 3. Surface time- and zonal-mean (a) zonal velocity, (b) turbulent zonal velocity, and (c) zonal stress, as a function of the Rayleigh number, as diagnosed from the numerical model. The sign of the turbulent zonal velocity is controlled by \bar{u} , which causes the ragged appearance of the contours. Both (a and b) use the same color scale. The intersection of the tangent cylinder and ocean surface is shown as the faint dashed lines.

The zonal flow field can be split into two main parts: a time-mean and a fluctuating turbulent component, \bar{u} and u' , respectively. We use the term turbulence to describe random fluctuations to the mean flow due to eddies in the velocity field. The magnitude of the turbulent velocities—the square root of the eddy variance—is shown in Figure 3b. It is shown in a slightly nontraditional form where the sign of the zonal turbulent velocities is controlled by the direction of mean flow. The reasoning for this will become evident in the next section. For now, there are two important things to note. First, the magnitude of turbulence increases with Rayleigh number, which is expected as the convective forcing becomes stronger. The second is that the turbulent velocities are in general weaker than the mean flow field, except in the highest Ra simulations. In particular, the strength of low-latitude turbulence becomes significantly larger than the mean flow when $Ra \gtrsim 1.5 \times 10^7$. This feature is essential to one of the main results in the next section—the reversal of the ice-ocean torque at high Rayleigh numbers.

3. The Ice-Ocean Torque

Now that we have examined the surface velocity field in detail, we turn to the surface stresses and resulting torque that the ocean exerts on the ice shell. The zonal-mean zonal stresses themselves, shown in Figure 3c, are certainly not large at only a few Pa (the yield strength of cold, intact ice is ~ 1 MPa). Only when integrated over the surface do the ocean-induced stresses become significant.

The ice-ocean torque has three components in the reference frame rotating with Europa, but for the present study, we focus on the axial component, \mathcal{T}_z , which is aligned with the rotation axis. This only depends on the meridional stress component evaluated at the surface (Appendix A),

$$d\mathcal{T}_z = \tau_\phi r \cos \theta dA, \quad (4)$$

where the area element $dA = r^2 \cos \theta d\theta d\phi$. The total torque is given by the integral over the surface at radius r ,

$$\mathcal{T}_z = 2\pi r^3 \int_{-\pi/2}^{\pi/2} \overline{\tau_\phi \cos^2 \theta} d\theta, \quad (5)$$

where the overbar operator denotes a zonal-mean (Equation A5). The torque can be written in terms of the near-surface velocity components by substituting the zonal-mean of the zonal stress component in Equation 2,

$$\mathcal{T}_z = 2\pi r^3 \rho_o c_D \int_{-\pi/2}^{\pi/2} \overline{u|u_h|} \cos^2 \theta d\theta, \quad (6)$$

where we assume that the density ρ_o at the surface bounded by r is constant. In Appendix B, we show that the velocity product in the above expression can be approximated by either the sum or product of the mean (overbar) and turbulent (primed) zonal kinetic energy densities, \overline{KE} and $\overline{KE'}$, respectively, depending on whether the turbulent velocities or mean velocities dominate the kinetic energy budget. If we neglect the mean and turbulent meridional velocity components, the torque can then be approximated as,

$$\mathcal{T}_z \sim 8\pi r^3 c_D \int_0^{\pi/2} [\overline{KE} + \overline{KE'}] \text{sgn}(\bar{u}) \cos^2 \theta d\theta, \quad (7)$$

in the quasi-linear regime, $|u'/\bar{u}| < 1$, and

$$\mathcal{T}_z \sim 16\pi r^3 c_D \int_0^{\pi/2} (\overline{KE} \overline{KE'})^{1/2} \text{sgn}(\bar{u}) \cos^2 \theta d\theta, \quad (8)$$

in the nonlinear regime, $|u'/\bar{u}| > 1$. Here, we define the zonal-mean zonal kinetic energy densities,

$$\{\overline{KE}, \overline{KE'}\} \equiv \frac{1}{2} \rho_o \{\bar{u}^2, \overline{(u')^2}\}, \quad (9)$$

the signum function,

$$\text{sgn}(\bar{u}) = \begin{cases} -1 & \text{if } \bar{u} < 0, \\ 0 & \text{if } \bar{u} = 0, \\ 1 & \text{if } \bar{u} > 0, \end{cases} \quad (10)$$

and we have further assumed zonal symmetry about the equator. By definition, both kinetic energy components are positive. The sign of the torque in Equation 9 then only depends on the direction of the zonal-mean zonal velocity. This is accounted for by $\text{sgn}(\bar{u})$, which changes sign depending on the jet direction. Notably, in the absence of a mean zonal flow, $\bar{u} = 0$, there is no zonal-mean stress, $\bar{\tau}_\phi = 0$, and consequently, no net torque. While the magnitude of the torque depends on both the turbulent and mean components of the zonal kinetic energy density, a net torque can only exist in the presence of a mean flow at that latitude.

3.1. Torque Derived From the GCM

In Figure 4a, we show the torque calculated from our simulations. The magnitude of the exact torque, calculated with the numerical stress output from the MITgcm and Equation 5, generally increases with the Rayleigh number of the ocean. The sign of the torque, though, switches from prograde to retrograde at around $Ra \sim 1.5 \times 10^7$, associated with the broad reversal of the low-latitude jet shown in Figures 2 and 3. Two separate approximations to the torque are also shown, calculated using Equations 7 and 8 with \overline{KE} and $\overline{KE'}$ as diagnosed from the model's velocity field. These approximations are applied globally, regardless of their validity, for illustration. The torque calculated with Equation 7, which is appropriate in the quasi-linear regime where $|u'/\bar{u}| < 1$, reproduces both the magnitude and sign of the exact torque, especially at low Ra . It overestimates the exact torque for the highest Ra simulations, particularly near the zero crossing. The torque calculated with Equation 8, which is valid in the nonlinear regime where $|u'/\bar{u}| > 1$, consistently underestimates the numerical solution at low Ra , but provides a much better reproduction of the numerical torque at high Ra and also captures the sign reversal.

The separate contributions of the mean flow and eddy field to the approximate torque in Equation 7 are also plotted in Figure 4a. The mean kinetic energy component is the dominant contributor to the torque for low Ra , while turbulence takes over at high Ra . Most notably, the figure shows that the torque reversal cannot be replicated by considering only \overline{KE} , which exclusively leads to prograde torques. Kinetic energy due to the turbulent convecting eddy field is therefore the primary control on the torque reversal that occurs at high Rayleigh numbers. It does this by amplifying the drag magnitude at low latitudes, where the zonal-mean zonal flow is subrotating. This can be seen by comparing Figures 3a and 3b.

Figure 4b shows the ratio of the meridional average of $\overline{KE'}$ to \overline{KE} , which is less than 1 until about $Ra \sim 10^7$. This increase in the kinetic energy ratio is associated with the reduction of the prograde torque and eventual

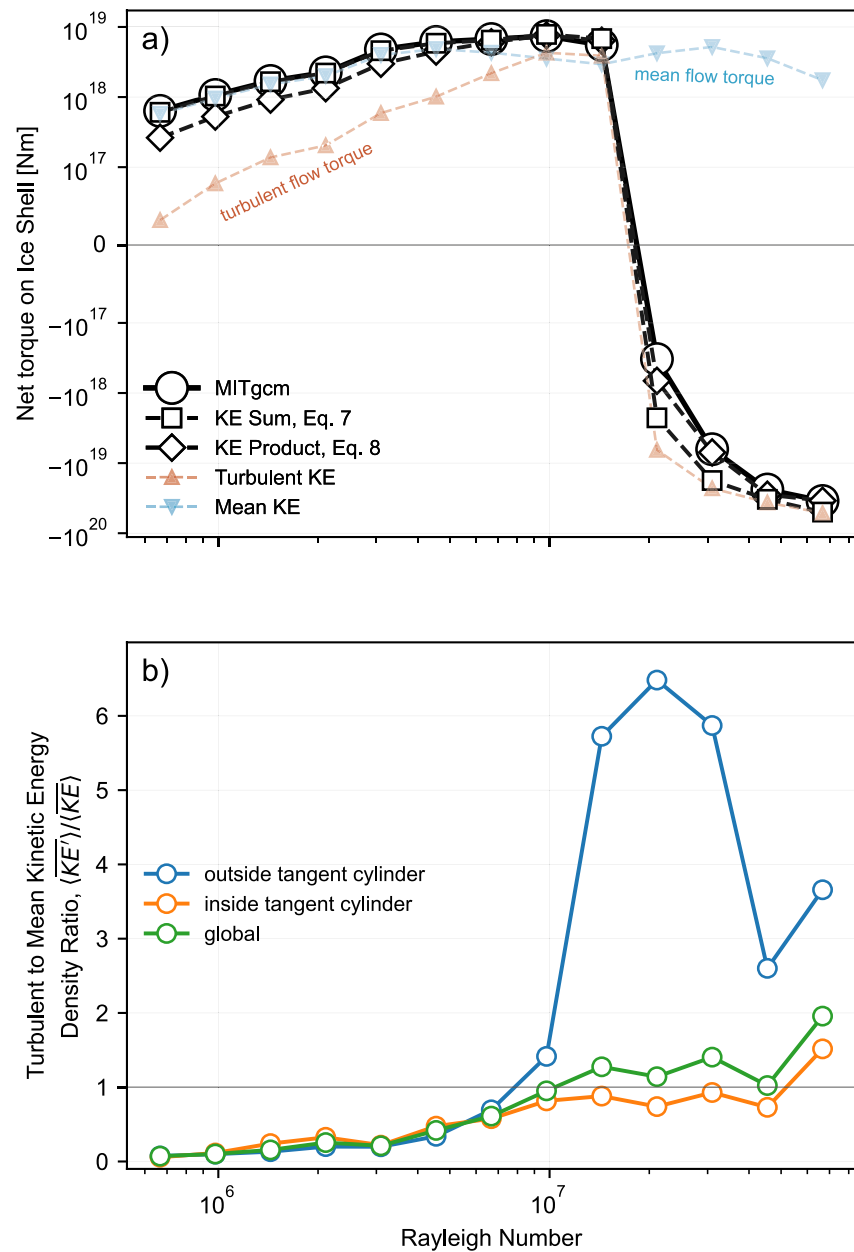


Figure 4. (a) The ice-ocean torque as a function of Rayleigh number, calculated using Equation 5 (solid line), and Equations 7 and 8 (black dashed lines). The torque calculated using the sum of the kinetic energy densities (Equation 7) and that calculated using the product (Equation 8) are denoted by squares and diamonds, respectively. The mean and turbulent contributions to the axial torque are shown by the faint blue and red curves, respectively. (b) The ratio of the zonal- and meridional-mean turbulent to mean kinetic energy densities. Each curve denotes the ratio for different regions of the meridional mean.

reversal to retrograde, shown in Figure 4a. It is also the point at which the numerical experiments switch from the quasi-linear to nonlinear regime, explaining why Equation 8 is better than Equation 7 at reproducing the torque when $Ra \gtrsim 1.5 \times 10^7$. When applied in their appropriate regime, Equations 7 and 8 both capture the order of magnitude and sign change of the numerical torque. Equations 7 and 8 are therefore useful approximations in calculating the ice-ocean torque if the surface velocity structure is known, especially given the level of detail required at this stage. Studies that do not apply quadratic drag can use 7 and 8 to roughly estimate the associated torque in their model, though this will likely provide an overestimate unless the drag term (2) is small enough to not impact the numerical simulation.

3.2. Torque Scaling Analysis

The torque calculations in the previous section use the surface stress and velocity fields from our numerical model. As mentioned in Section 2, the Ekman and Rayleigh numbers used in the numerical setup (Tables 1 and 2) are far from the realistic values of $Ek \sim 10^{-12}$ and $Ra \sim 10^{25}$ (Soderlund, 2019). This begs the question: does our numerical model predict realistic torque magnitudes? From our expressions for the approximate torque, Equations 7 and 8, we see that the answer to this question boils down to how well the numerical model predicts the mean and turbulent kinetic energy densities of the ocean near surface, as well as the latitudinal structure of the zonal jets. This is by no means a trivial problem, and we shall proceed here by making crude approximations in an attempt to calculate, to order of magnitude, the ice-ocean torque for an arbitrary ocean that exhibits zonal jets.

We start by assuming nothing about the specific functional form of the surface velocity field, except that the strongest jets occur outside of the tangent cylinder, θ_{tc} , and the velocity/kinetic energy field is symmetric about the equator. Combined with the small angle approximation $\cos^2\theta \sim 1$, these assumptions reduce Equation 7 to,

$$\mathcal{T}_z \sim 8\pi r^3 c_D \int_0^{\theta_{tc}} [\overline{KE} + \overline{KE'}] \text{sgn}(\bar{u}) d\theta. \quad (11)$$

Limiting the integral to outside the tangent cylinder is reasonable for the low Ra simulations, but not in the high Ra regime, where significant strong zonal flow exists at high latitudes (Figures 2 and 3). The following analysis is therefore only applicable to the quasi-linear regime of rotating convection where jets are “trapped” at low latitudes (Miquel et al., 2018). Though the tangent cylinder creates a convenient reference latitude for the integral, any small latitude will do, provided the majority of the zonal-mean zonal kinetic energy field occurs there.

Next, we note that $\text{sgn}\bar{u}$ can be expressed using the Heavyside function $H(\bar{u})$,

$$\begin{aligned} \mathcal{T}_z &\sim 8\pi r^3 c_D \int_0^{\theta_{tc}} [\overline{KE} + \overline{KE'}] [2H(\bar{u}) - 1] d\theta \\ &\sim 8\pi r^3 c_D \left[2 \int_0^{\theta_{tc}} [\overline{KE} + \overline{KE'}] H(\bar{u}) d\theta - \int_0^{\theta_{tc}} [\overline{KE} + \overline{KE'}] d\theta \right], \end{aligned} \quad (12)$$

where,

$$H(x) = \begin{cases} 0 & \text{if } x < 0, \\ 1/2 & \text{if } x = 0, \\ 1 & \text{if } x > 0. \end{cases} \quad (13)$$

This is useful because $H(\bar{u})$ in Equation 12 essentially acts to filter out any retrograde flow. Using this fact, we define four new quantities:

$$\begin{aligned} (\langle \overline{KE} \rangle, \langle \overline{KE'} \rangle) &= \frac{1}{\theta_{tc}} \int_0^{\theta_{tc}} (\langle \overline{KE} \rangle, \langle \overline{KE'} \rangle) d\theta, \quad \text{and} \\ (\langle \overline{KE} \rangle_+, \langle \overline{KE'} \rangle_+) &= \frac{1}{\theta_{tc}} \int_0^{\theta_{tc}} (\langle \overline{KE} \rangle, \langle \overline{KE'} \rangle) H(\bar{u}) d\theta. \end{aligned} \quad (14)$$

The $\langle \rangle$ operator denotes a meridional mean (Appendix A), in this case taken between 0 and θ_{tc} , again with the assumption of zonal symmetry about the equator. The first expression is therefore the meridional average of the near-surface zonal-mean and turbulent kinetic energy densities outside of the tangent cylinder. The second expression is the meridional average of the zonal-mean and turbulent kinetic energy densities associated with eastward zonal-mean flow, denoted by the + subscript. We can relate the two with,

$$\begin{aligned} \langle \overline{KE} \rangle_+ &= \xi \langle \overline{KE} \rangle, \quad \text{and} \\ \langle \overline{KE'} \rangle_+ &= \xi' \langle \overline{KE'} \rangle, \end{aligned} \quad (15)$$

where ξ and ξ' are factors between 0 and 1 that indicate the fraction of the near-surface kinetic energy field that is associated with superrotation. The number, width, and strength of the jets outside the tangent cylinder all control ξ and ξ' . Substituting Equation 14 into Equation 12, along with Equation 15, gives,

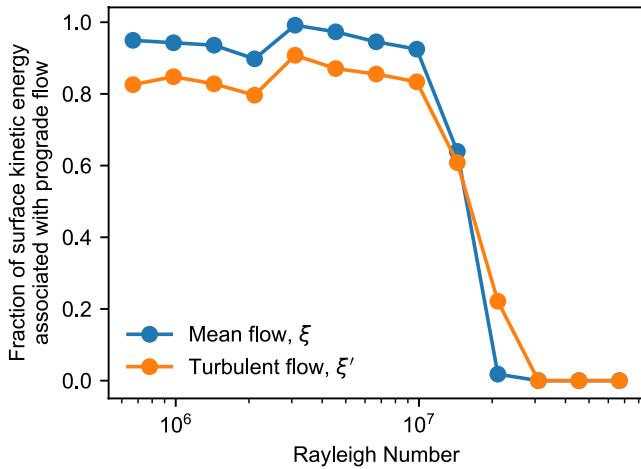


Figure 5. The fraction of surface zonal kinetic energy associated with superrotating (prograde) flow outside of the tangent cylinder (Equation 15) as a function of Rayleigh number.

correlated and typically $\xi/\xi' \sim 1$. In the quasi-linear regime, $\xi \sim 0.95$, and in the highest Ra simulations $\xi = 0$ because there is only retrograde flow outside of the tangent cylinder. These results justify our next assumption, that $\xi \sim \xi'$, at least outside of the tangent cylinder. This allows us to simplify Equation 16 further to,

$$\mathcal{T}_z \sim 8\pi r^3 c_D \theta_{ic} (2\xi - 1) \langle \overline{KE} \rangle \left[1 + \frac{\langle \overline{KE'} \rangle}{\langle \overline{KE} \rangle} \right], \quad (17)$$

reducing the problem to now only three properties. By definition, $0 \leq \xi \leq 1$, so the last step in generalizing the ice-ocean torque is to consider the kinetic energy of the ocean.

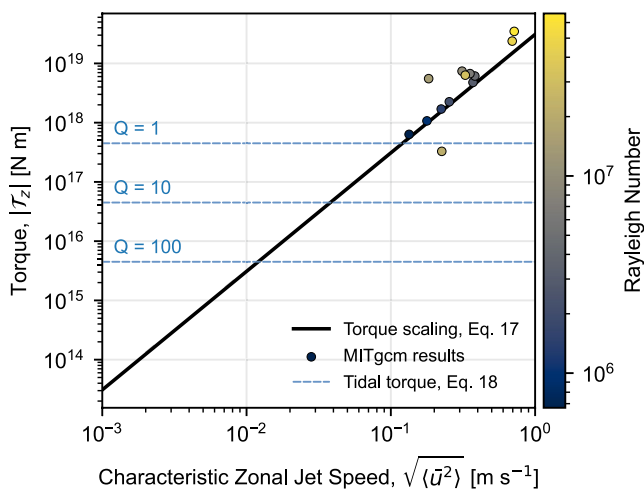


Figure 6. Europa's ice-ocean torque as a function of the meridional average of the surface zonal-mean jet speed outside the tangent cylinder. The numerical results are given by the dots, and the solid line gives the torque calculated using the scaling law in Equation 17 for $c_D = 0.002$, $\xi = 0.95$, and $\langle \overline{KE'} \rangle = 0$. The dashed blue lines show the tidal torque on a 20-km-thick ice shell for different Q values of ice.

$$\mathcal{T}_z \sim 8\pi r^3 c_D \theta_{ic} (2\xi - 1) \langle \overline{KE} \rangle \left[1 + \frac{(2\xi' - 1) \langle \overline{KE'} \rangle}{(2\xi - 1) \langle \overline{KE} \rangle} \right]. \quad (16)$$

We have therefore reduced the problem of the ocean-induced torque to four main unknown properties of the ocean: the surface meridional- and zonal-mean kinetic energy densities from mean flow and turbulence, $\langle \overline{KE} \rangle$ and $\langle \overline{KE'} \rangle$, and the fraction of those associated with superrotation, ξ and ξ' .

In the quasi-linear regime, we can neglect the second term in Equation 16 because the contribution of turbulence to the axial torque is small, as already demonstrated in Figure 4. However, if the ocean surface outside the tangent cylinder has equal partition between east and west mean flow, such that $\xi = 1/2$ and the mean-flow contribution to the torque in Equation 16 goes to zero, then the net torque will only be zero if $\xi' = 1/2$ as well. This condition requires ξ and ξ' to be highly correlated at least when ξ approaches $1/2$. Fortunately, these are all quantities we can diagnose from our numerical simulations.

Figure 5 shows how ξ and ξ' vary outside of the tangent cylinder as a function of Rayleigh number in the numerical results. We see that the two are well correlated and typically $\xi/\xi' \sim 1$. In the quasi-linear regime, $\xi \sim 0.95$, and in the highest Ra simulations $\xi = 0$ because there is only retrograde flow outside of the tangent cylinder. These results justify our next assumption, that $\xi \sim \xi'$, at least outside of the tangent cylinder. This allows us to simplify Equation 16 further to,

We have seen in Figure 4b that the ocean's kinetic energy associated with zonal flow is dominated by the mean flow when Ra is low. To estimate the torque in this regime, we can then neglect the second term in Equation 17 and only require an estimate of $\langle \overline{KE} \rangle$. Showman et al. (2011) developed analytical scaling laws to predict the magnitude of the zonal flow speed for superrotation on the giant planets, though none currently exist for Europa and the other ocean worlds. We therefore simply take $\langle \overline{KE} \rangle$ as a free parameter.

Figure 6 shows the axial torque magnitude calculated using Equation 17 as a function of the characteristic zonal-mean zonal velocity, neglecting the contribution of turbulence, $\langle \overline{KE'} \rangle = 0$, and setting the superrotating fraction of the surface mean flow outside the tangent cylinder to $\xi = 0.95$ as determined from Figure 5. Figure 6 also shows the numerical results, indicating that our scaling law accurately predicts the torque in the lowest few Ra simulations, while underestimating the torque for the higher Ra simulations except for one, which it overpredicts. The better fit for low Ra is not surprising given that we started with the quasi-linear drag law (7), used ξ as determined from our simulations with low Ra, and that we restricted the torque integral outside the tangent cylinder where most of the jets are, an assumption that is only true for quasi-linear convection (Figure 3, also see Miquel et al. (2018)). The one simulation that falls below the line occurs near the zero-crossing between positive and negative torques. Equation 17 therefore provides a lower limit on the ice-ocean torque, except during the sign transition.

4. Discussion

4.1. Magnitude of Torque

The magnitude of the torque is critical in assessing how much the ocean can drive changes in the rotation of the ice shell. If our simulations predict both mean and turbulent zonal speeds that are too large, then a more realistic torque may be smaller than that calculated using only the numerical results in Figure 4. For super-rotation, the jets here are driven by the turbulent (eddy) flux of angular momentum away from the rotation axis, which must be balanced by the viscous/drag fluxes of angular momentum (Böning et al., 2023; Kaspi et al., 2009). This essentially means that, roughly speaking, $\langle KE \rangle$ is a function of $\langle KE' \rangle$, the fluid's viscosity, ν , and the drag coefficient at the boundaries, c_D . We leave determining this relationship for future work (e.g., Jansen et al., 2022).

To understand how significant the ice-ocean torque may be, we compare it in magnitude to the tidal torque on the ice shell. According to Goldreich and Mitchell (2010, their Equation 16), the tidal torque can be expressed as,

$$\tau_z^{tide} = \frac{576}{5} \pi e^2 \left(\frac{1 + \tilde{\nu}}{5 + \tilde{\nu}} \right) \frac{h_2^2}{Q} \left(\frac{n^2 R^3}{GM} \right)^2 \mu H R^2, \quad (18)$$

where $e = 0.01$ is Europa's orbital eccentricity, $\tilde{\nu} = 1/3$ and $\mu = 3.5$ GPa are Poisson's ratio and the shear modulus of ice, respectively, $h_2 \sim 1$ is the displacement tidal Love number, Q is the tidal quality factor, $n = 2.05 \times 10^{-5} \text{ s}^{-1}$ is the orbital mean motion, G is the universal gravitation constant, M is Europa's mass, and $H \sim 20$ km is the ice shell thickness (e.g., Howell, 2021). Values of this torque for $Q = 1, 10$, and 100 are shown against our scaling law and numerical results in Figure 6.

All of our numerical simulations, bar one, predict torques greater than the most dissipative (smallest Q) ice shells. This roughly corresponds to a characteristic zonal flow speed exceeding 10 cm s^{-1} . Extrapolating further using our scaling law, we see that the ice-ocean torque balances the tidal torque if $Q = 10$ and $\sqrt{\langle \bar{u}^2 \rangle} \approx 5 \text{ cm s}^{-1}$ or if $Q = 100$ and $\sqrt{\langle \bar{u}^2 \rangle} \approx 1 \text{ cm s}^{-1}$. As a reminder, the scaling law applies only to the quasi-linear regime of convection. More turbulent flow can potentially increase the axial torque by up to a factor of 2 (Equation 17, assuming the flow is still quasi-linear).

Zonal-mean zonal jet speeds of 1 cm s^{-1} to 100 cm s^{-1} are certainly not out of the question, but whether the tidal torque exceeds the ice-ocean torque also depends on the Q and thickness of the ice shell. At the current state of knowledge, the most likely ice shell thickness is ~ 20 km according to Howell (2021), though other estimates have been put forth. The tidal Q value is related to the viscosity of the ice shell, which is another highly uncertain parameter that can span many orders of magnitude. Given how poorly these are constrained, it is possible that the ice-ocean torque due to ocean dynamics could be comparable to the tidal torque in most cases. One takeaway seems clear: ocean dynamics that manifest in zonal jets should be incorporated into future studies concerned with the torque balance on and rotation of Europa's ice shell (e.g., Baland & Van Hoolst, 2010; Bills & Scott, 2022; Bills et al., 2009; Greenberg & Weidenschilling, 1984; Rambaux et al., 2011; Van Hoolst et al., 2008). Our scaling analysis suggests that the absolute lower limit for the ice-ocean torque to be significant is $\sim 1 \text{ cm s}^{-1}$. Sluggish jets of only a few mm s^{-1} are unlikely to give rise to a meaningful torque, no matter the properties of the ice shell.

At first glance, our results appear to imply that an increase in the buoyancy forcing/Rayleigh number of the ocean always leads to an increasingly strong torque except near the zero-crossing. This cannot continue indefinitely, though; at even higher Ra than simulated here, buoyancy forcing becomes so strong that rotation has no effect on the solution, and convection proceeds randomly (e.g., Gastine et al., 2015). No zonal-mean flow develops in this case, meaning that even with strong turbulence and drag, no time-mean net torque can exist (Equations 7 and 8, and subsequent discussion).

4.2. Reversal of Torque

Our numerical results show that if the Rayleigh number of the ocean becomes large enough, buoyancy forces overcome inertial forces by such a margin that the equatorial zonal jet reverses direction from prograde to retrograde. Unlike Earth, Europa's ocean is not subject to seasons, but may be subject to tidal heating variations modulated by periodic changes in orbital eccentricity (e.g., Běhouňková et al., 2021; Hussmann & Spohn, 2004) and distance from Io and Ganymede (Hay et al., 2020, 2022). Any changes in tidal heating over time will alter Europa's Rayleigh number and consequently the dynamical behavior of its ocean. This will at least alter the magnitude of the torque that the ice shell experiences, and we speculate that this could potentially reverse the torque direction (or remove it altogether) if the heating rates were sufficient.

Tectonic stresses would build up in the ice shell if a torque reversal occurred over a sufficiently short timescale. For fracturing of the ice to occur, the shell requires an angular displacement of at least 10° , relative to Jupiter, for elastic stresses to approach the yield strength of ice (Goldreich & Mitchell, 2010, see their Equation 12). This corresponds to an elastic restoring torque in the ice shell of at least 10^{20} N m. We estimate that characteristic jet speeds of 1 m s^{-1} to 10 m s^{-1} are required to approach such a large torque. It remains questionable as to whether Europa's interior is energetic enough to drive such fast zonal flows (Jansen et al., 2022). However, we again emphasize that some of Europa's geological features are consistent with episodic nonsynchronous rotation, but potentially not continuous (Crawford & Pappalardo, 2006; McEwen, 1986; Selvens, 2009; Spaun, 2002). The torque induced by convectively driven ocean dynamics may provide a natural mechanism to do this, or at least alter the long-term torque balance on the ice shell as the thermal state of the interior evolves.

4.3. Angular Momentum Flux in the System

If Europa's interior was perfectly spherical (i.e., no tides or oblateness), then it may seem like that the ice-ocean torque will indefinitely spin up the ice shell. This is not the case though. The velocity in Equation 2 is technically the relative velocity between the ocean surface and ice shell. There is therefore some equilibrium where the ice shell (and solid interior) differentially rotate so that there is no longer a net torque. Europa is not perfectly spherical though—the solid interior and ice shell are deformed by rotation and tides into a triaxial figure. Any misalignment between them, as well as with Jupiter, leads to gravitational and pressure torques that act to return them to an aligned state. The flux of angular momentum between the seafloor and ice shell therefore ultimately comes from Europa's orbit.

4.4. Observations

If ocean currents provided the only torque acting on Europa's ice shell, any detection of nonsynchronous rotation by a spacecraft would be a direct detection of ocean dynamics. This could potentially be used to back-out properties of the ocean, such as its Rayleigh number and mean velocity, by using models like that used here. In reality, this would be challenging because of other torques acting on the ice shell, such as that due to tides (Greenberg & Weidenschilling, 1984) and elasticity of the ice shell (Goldreich & Mitchell, 2010), for example, which all depend on other poorly constrained parameters. The potential remains, however, if enough of the properties of the ice and interior can be constrained through other investigations. The upcoming Europa Clipper mission will be best placed to do this in the future.

4.5. Jet Characteristics in the Asymptotic Regime

Christensen (2002) argued that in their free-slip numerical experiments of rotating convection, the time-mean solutions entered an asymptotic regime where only the strength of forcing controlled the steady-state outcome, and the viscosity played little to no role. If such a limit exists, how will it affect the results presented here? This essentially requires us to understand how vanishing Ekman number alters the strength $\left(\overline{KE}\right)$, and number/width (ξ) of zonal jets.

It is well established that inside the tangent cylinder, jet width is controlled by the Rhines scale as defined in Equation 6 from Heimpel and Aurnou (2007), which takes into account the curvature of the domain (i.e., the topographic- β effect, also see Bire et al., 2022). Outside of the tangent cylinder, which is where we assume the most significant torque to occur (at least in the quasi-linear regime), the Rhines scale severely underpredicts

the jet width, a consequence of the discontinuity in ocean thickness described in Figure 1. In fact, the majority of numerical simulations form no more than one to two jets outside the tangent cylinder (e.g., Bire et al., 2022; Kaspi et al., 2009; Kverka & Čadež, 2022; Soderlund, 2019), even across a range of Ekman numbers. We anticipate then that the number of jets outside the tangent cylinder is unlikely to exceed one to two when considering more realistic Ekman and Rayleigh numbers. This means that we do not expect ξ to be strongly affected by decreasing Ek, provided that Ra is simultaneously adjusted to keep the solution in the same convective regime (see Figure 1 in Soderlund, 2019).

The jet speed, roughly parameterized here by $\langle \overline{KE} \rangle^{1/2}$, is also a key unknown parameter in controlling the torque. Showman et al. (2011) reason that, at least for giant planets in the asymptotic regime, the kinetic energy of the zonal flows will depend on the balance between the eddy flux of angular momentum into the jet and the viscous damping due to eddy, rather than molecular, diffusion. They tentatively find that the jet speed scales weakly with the basal heat flux in this regime. In our case, where the upper boundary is solid, the same scaling may not apply due to boundary layer drag. This makes it a challenge to estimate the near-surface jet speed in the limit of vanishing Ekman number. Clearly, constraining this relationship is an important topic for future work.

4.6. Shortcomings and Future Work

While our study makes the first attempt at estimating the ice-ocean torque due to convectively driven ocean dynamics, there are a number of simplifications that must be highlighted.

4.6.1. Simplification of Drag

The frictional boundary layer between the ice and ocean will be turbulent if the Reynolds number at the boundary layer is sufficiently high. In this regime, the mean velocity profile within the bulk of the frictional boundary layer is well approximated by the logarithmic Law of the Wall (Von Karman, 1931). The quadratic bottom/top drag and its associated coefficient used in our study, c_D , come directly from this logarithmic relationship (e.g., Shirasawa & Ingram, 1991, Equation 5),

$$c_D = \left[\frac{k}{\ln(z_r/z_0)} \right]^2, \quad (19)$$

where $k = 0.4$ is von Karman's constant, z_r is the distance from the boundary where c_D is evaluated, and z_0 is the roughness length scale of the solid boundary. Our expression for drag (Equation 2) therefore only accounts for the friction that arises due to the hydraulic roughness of the ice-ocean interface, known as skin friction. Roughness here represents obstacles to the flow that have a vertical extent much smaller than the boundary layer thickness, $\delta = \text{Ek}^{1/2}D$. For realistic European parameters using $\nu \approx 2 \times 10^{-6} \text{ m}^2 \text{ s}^{-1}$ and a near-boundary flow speed of $U = 0.01 \text{ m s}^{-1}$, the boundary layer Reynolds number is roughly $\text{Re}_{bl} = U\delta/\nu \sim 1500$, suggesting that the frictional boundary layer is likely turbulent, even in the absence of any roughness. Surface roughness itself can cause the flow to become turbulent near the boundary for even smaller U (e.g., Shirasawa, 1986; Shirasawa & Ingram, 1991), but we stress that our chosen drag law implies that the frictional boundary layer is turbulent, which is an assumption.

If there are more significant topographical variations at the ocean top and bottom, the total drag will increase due to form drag (i.e., the normal force exerted by flow at a non-horizontal interface, Arya, 1975; Steele et al., 1989). This is different to skin friction as the obstacles to flow are comparable to or much greater than the boundary layer thickness δ . Drag induced by atmospheric flow over the Himalayan and Rocky mountain chains is a good example of this (Madden & Speth, 1995). Any basal topography, especially with sharp discontinuities (e.g., normal faults that extend into the ice-ocean interface) could significantly contribute, either positively or negatively, to the ice-ocean torque. If such topography existed, though, its lifetime is expected to be short due to viscous relaxation of the ice (Nimmo, 2004) and the ice-pump effect (Lewis & Perkin, 1986). Seafloor bathymetry may be a more promising source of form and mountain drag on the ocean.

4.6.2. Salinity and Other Ocean-Forcing Mechanisms

The only forcing in our numerical model is a buoyancy flux at the seafloor where the ocean is heated and at the ice-ocean interface where it is cooled. This is similar to several other studies (Amit et al., 2020; Bire et al., 2022;

Kvorka & Čadež, 2022; Soderlund, 2019; Soderlund et al., 2014). We do not consider tidal forcing (e.g., Hay & Matsuyama, 2019; Rovira-Navarro et al., 2020; Tyler, 2008), magnetic forcing (Gissinger & Petitdemange, 2019), or ocean salinity (Ashkenazy & Tziperman, 2021; Zeng & Jansen, 2021; Zhu et al., 2017). Salt must exist at some concentration in Europa's ocean (e.g., Zimmer et al., 2000) though its influence on the most energetic flow remains questionable (Jansen et al., 2022). Tidal forcing due to Europa's obliquity can drive strong currents (1 cm s^{-1} to 10 cm s^{-1}) via planetary Rossby waves provided the obliquity is large enough (Chen & Nimmo, 2011; Chen et al., 2014; Hay & Matsuyama, 2019; Tyler, 2008), but small deviations in ocean thickness away from a uniform state may reduce this particular tidal response (Rovira-Navarro et al., 2020). The influence of tides on the mean flow remains an open question and has received recent attention by Vincent et al. (2022), though their model does not self-consistently account for convective dynamics. Gissinger and Petitdemange (2019) found that Jupiter's magnetic field can also drive a low-latitude retrograde jet in Europa's ocean, and they were the first to suggest that this flow may exert a net torque on the ice shell. While we do not include the significant complication of the magneto-hydrodynamical equations in our model, our scaling laws can still be applied to their numerical results.

4.6.3. Deformation of the Ocean Surface

The ocean surface is deformable in our MITgcm setup (Campin et al., 2004), rather than the rigid-lid condition that is commonly applied in simulations of rotating convection. Europa's ice shell is certainly not completely rigid because it is expected to be thin compared to the radius of the body (e.g., Howell, 2021; Wahr et al., 2006). The shell's ability to resist deformation depends not only on its thickness and shear modulus, but also strongly on the wavelength of the forcing. For example, the ice shell is weak to long-wavelength tidal forcing, but will be strong against small-scale internal loading from rising, narrow plumes. Our choice to use a deformable free surface is therefore a reasonable approximation for long-wavelength dynamics, but a poor one for small-wavelengths. This choice also means that our model permits the existence of surface waves, which would otherwise be filtered out by the rigid-lid condition. In the future, we will modify the MITgcm to include the surface pressure exerted by an overlying elastic lid (e.g., Beuthe, 2016), which will effectively act to remove the smallest scales of ocean deformation.

4.6.4. Numerical Limitations

Finally, and perhaps most severely, our model is limited by the computing resources available. We select a kinematic viscosity of $61.6 \text{ m}^2 \text{ s}^{-1}$ in order to maintain stability of the numerical solution at the resolution of our model. This is only around three times higher than recent estimates of the eddy viscosity (Ashkenazy & Tziperman, 2021), but many orders of magnitude greater than the molecular viscosity of water. Our results are therefore only meaningful in lieu of the scaling laws, which dictate our choice of Rayleigh number based on the Ekman number chosen (Soderlund, 2019). Future work must move past some of these limitations by using different or higher-resolution models on smaller domains (e.g., Ashkenazy & Tziperman, 2021; Bire et al., 2022), though care must be taken to ensure that wave structures are still resolved at the highest latitudes. We stress that, in general, our results and methodology are applicable to any moon where the dynamics of the system are dominated by east-west zonal jets.

5. Conclusions

We have for the first time estimated the time-mean stress field and resulting torque that must exist between the flowing ocean and solid ice shell of Europa. Perhaps unintuitively, the stress field due to alternating zonal jets does not necessarily cancel out once integrated over the entire surface. This means that it is likely that ocean dynamics that manifest in east-west jets exert a net unidirectional torque on the ice shells of Europa and other ocean worlds.

We simplify the torque calculation to roughly estimate the magnitude of the ice-ocean torque as a function of the zonal- and meridional-mean kinetic energy fields. The analysis suggests that a minimum speed of 1 cm s^{-1} is required for the ice-ocean torque to be comparable to the tidal torque exerted by Jupiter. A jet speed of 10 cm s^{-1} or greater produces a torque that likely dominates the tidal torque. These jet speeds are reasonable, suggesting that the ice-ocean torque may play a role in the rotation of Europa's ice shell over time.

The scaling analysis shows that strengthening of turbulent convection reverses the equatorial jet and resulting torque such that it acts against the direction of rotation. The reversal occurs when the thermal buoyancy forcing becomes large enough to drive highly turbulent convection. If the energetic state of Europa's interior has changed

sufficiently over time, perhaps due to the depletion of radioactive heat producing elements or changes in tidal forcing, it is possible that a reversal has taken place. We speculate that this provides a novel mechanism to stop, start, and even reverse nonsynchronous rotation of the ice shell.

Our study makes a first attempt at estimating the ice-ocean torque in the most general case. Forcing due to tides, salt, and magnetism are not taken into account, though they may play a role in influencing the time-mean zonal jets that give rise to the torque. A key next step is understanding how these different forcing fields impact the time-mean dynamics of the ocean when coupled with convective flow as well as the fundamental controls on the strength, number, and latitudes of zonal jets.

Appendix A: Definitions

A1. Vector Definitions

The velocity and stress fields are defined in spherical coordinates as,

$$\mathbf{u} = u\hat{e}_\phi + v\hat{e}_\theta + w\hat{e}_r, \quad (\text{A1})$$

$$\boldsymbol{\tau} = \tau_\phi\hat{e}_\phi + \tau_\theta\hat{e}_\theta + \tau_r\hat{e}_r, \quad (\text{A2})$$

where the spherical unit vectors in longitude ϕ , latitude θ , and radial position r are related to the Cartesian reference frame rotating with Europa via,

$$\begin{bmatrix} \hat{e}_r \\ \hat{e}_\theta \\ \hat{e}_\phi \end{bmatrix} = \begin{bmatrix} \cos\theta\cos\phi & \cos\theta\sin\phi & \sin\theta \\ -\cos\phi\sin\theta & -\sin\phi\sin\theta & \cos\theta \\ -\sin\phi & \cos\phi & 0 \end{bmatrix} \begin{bmatrix} \hat{e}_x \\ \hat{e}_y \\ \hat{e}_z \end{bmatrix}. \quad (\text{A3})$$

The horizontal velocity field is defined as $\mathbf{u}_h \equiv (u\hat{e}_\phi, v\hat{e}_\theta)$, with a similar expression for horizontal stress. The axial component of the torque that arises from the boundary stress $\boldsymbol{\tau}$ acting over the spherical area element dA is,

$$d\mathcal{T}_z = (\mathbf{r} \times \boldsymbol{\tau}) \cdot \hat{e}_z dA = \tau_\phi r \cos\theta dA = \tau_\phi r^3 \cos^2\theta d\theta d\phi. \quad (\text{A4})$$

A2. Averaging Operators

We use typical definitions of various averaging operators to simplify our numerical and analytical analyses. These are the zonal-mean,

$$\bar{x} = \frac{1}{2\pi} \int_0^{2\pi} x d\phi, \quad (\text{A5})$$

and meridional-mean,

$$\langle x \rangle = \frac{1}{2\theta} \int_{-\theta}^{\theta} x d\theta'. \quad (\text{A6})$$

Appendix B: Analytical Torque

The torque depends on the product $u|u|$ (2). We simplify this using a Reynold's decomposition, splitting the zonal velocity into a time-average and time-variable component, \bar{u} and u' , respectively.

B1. Quasi-Linear Regime

We start by simplifying the absolute value of u ,

$$|\bar{u} + u'| \approx |\bar{u}| \left(\left(1 + \frac{u'}{\bar{u}} \right)^2 + \left(\frac{u'}{\bar{u}} \right)^2 \right)^{1/2}, \quad (\text{B1})$$

where we neglect \bar{v} . Next, we introduce the ratio of the turbulent velocities, $c = v'/u'$. This allows us to perform a Taylor series expansion assuming that u'/\bar{u} is small and that $c \lesssim 1$:

$$\begin{aligned} |\bar{u} + u'| &\approx |\bar{u}| \left(\left(1 + \frac{u'}{\bar{u}} \right)^2 + \left(\frac{cu'}{\bar{u}} \right)^2 \right)^{1/2}, \\ &\sim |\bar{u}| \left(1 + \frac{u'}{\bar{u}} + \frac{c^2}{2} \left(\frac{u'}{\bar{u}} \right)^2 \right), \end{aligned} \quad (\text{B2})$$

which is accurate to second order in u'/\bar{u} . The term in parenthesis must be positive for the above to remain correct, implying that,

$$1 + \frac{c^2}{2} \left(\frac{u'}{\bar{u}} \right)^2 \geq -\frac{u'}{\bar{u}}. \quad (\text{B3})$$

This positivity constraint is satisfied no matter the sign of u' or \bar{u} as the left-hand side is always positive and because we are in the quasi-linear regime where $|u'|/|\bar{u}| < 1$. The mean zonal drag in Equation 6 then depends on,

$$\begin{aligned} \overline{(\bar{u} + u')|\bar{u} + u'|} &\sim \overline{(\bar{u} + u')|\bar{u}| \left(1 + \frac{u'}{\bar{u}} + \frac{c^2}{2} \left(\frac{u'}{\bar{u}} \right)^2 \right)} \\ &= \bar{u}|\bar{u}| + \overline{u'|\bar{u}|} + \frac{c^2}{2} \overline{\left(\frac{u'}{\bar{u}} \right)^2 \bar{u}|\bar{u}|} + \overline{(u')^2 \frac{|\bar{u}|}{\bar{u}}} + \frac{c^2}{2} \overline{\left(\frac{u'}{\bar{u}} \right)^2 u'|\bar{u}|} \\ &= \bar{u}|\bar{u}| + \frac{c^2}{2} \overline{\left(\frac{u'}{\bar{u}} \right)^2 \bar{u}|\bar{u}|} + \overline{(u')^2 \frac{|\bar{u}|}{\bar{u}}}, \end{aligned} \quad (\text{B4})$$

where we use the fact that $\overline{(u')^n} = 0$ if n is an odd number. Using the identity $|x| = x \text{sgn}(x)$ and assuming that c^2 does not vary with longitude (i.e., u' and v' are always correlated as a function of latitude), the above expression simplifies to,

$$\overline{(\bar{u} + u')|\bar{u} + u'|} \sim \left[\bar{u}^2 + \overline{(u')^2} \left(1 + \frac{1}{2} c^2 \right) \right] \text{sgn}(\bar{u}). \quad (\text{B5})$$

Finally, when multiplying Equation B5 by ρ_o and c_D , we can see that the zonal-mean zonal bottom/top stress is related to the sum of the zonal-mean zonal kinetic energy density and turbulent zonal kinetic energy density at the ocean surface, modified by the direction of mean flow:

$$\overline{\tau_\phi} = c_D \rho_o \overline{(\bar{u} + u')|\bar{u} + u'|} \sim 2c_D \left[\overline{KE} + \overline{KE'} \left(1 + \frac{1}{2} c^2 \right) \right] \text{sgn}(\bar{u}). \quad (\text{B6})$$

Expressing the drag in this way is both useful and informative. There is no division by either u' or \bar{u} , so the drag is still defined if either quantity is zero. There are two terms both with distinct meanings. The first term is the drag only due to the zonal-mean zonal flow, while the second term is the contribution of turbulence to the drag. Turbulence must take part in contributing to bottom/top drag because it alters the absolute value on the left-hand side. Turbulence, though, is random and so cannot contribute to a net (i.e., east or west) zonal stress, unless there is a background mean flow. The inclusion of $\text{sgn}(\bar{u})$ accounts for this by switching the sign of the second term depending on the direction of the mean flow. Furthermore, we see that if there is no mean flow, $\bar{u} = 0$, but there is still turbulence, $\overline{(u')^2} > 0$, there cannot be any *net* drag at the boundary because $\text{sgn}(\bar{u}) = 0$, essentially turning off the second term. In the main manuscript, we neglect the meridional turbulent velocity component for simplicity by setting $c = 0$.

B2. Nonlinear Regime

When convection is strongly nonlinear, $|u'| > |\bar{u}|$, so we can instead write the absolute velocity as,

$$\begin{aligned} |\bar{u} + u'| &= |u'| \left(\left(1 + \frac{\bar{u}}{u'} \right)^2 + \left(\frac{v'}{u'} \right)^2 \right)^{1/2} \\ &= |u'| \left(\left(1 + \frac{\bar{u}}{u'} \right)^2 + c^2 \right)^{1/2} \\ &\sim |u'| \left((1 + c^2)^{1/2} + \frac{1}{(1 + c^2)^{1/2}} \frac{\bar{u}}{u'} + \frac{c^2}{2(1 + c^2)^{3/2}} \left(\frac{\bar{u}}{u'} \right)^2 \right) \end{aligned} \quad (\text{B7})$$

where we again use a Taylor series expansion in the last line, neglecting third-order terms and higher. As before, the term in parenthesis must be positive for the above to be true, meaning that,

$$1 + c^2 + \frac{c^2}{2(1 + c^2)} \left(\frac{\bar{u}}{u'} \right)^2 \geq -\frac{\bar{u}}{u'}. \quad (\text{B8})$$

As we are considering the nonlinear convection regime where $|u'| > |\bar{u}|$, this positivity constraint is satisfied no matter the sign of u' or \bar{u} because the left-hand side is always positive and greater than unity. In this case, the mean drag term instead depends on,

$$\begin{aligned} \overline{(\bar{u} + u')|\bar{u} + u'|} &\sim \overline{(\bar{u} + u')|u'| \left((1 + c^2)^{1/2} + \frac{1}{(1 + c^2)^{1/2}} \frac{\bar{u}}{u'} + \frac{c^2}{2(1 + c^2)^{3/2}} \left(\frac{\bar{u}}{u'} \right)^2 \right)} \\ &= \overline{(1 + c^2)^{1/2} (\bar{u}|u'| + u'|u'|)} + \overline{\frac{1}{(1 + c^2)^{1/2}} \left(\bar{u}^2 \frac{|u'|}{u'} + \bar{u}|u'| \right)} + \overline{\frac{c^2}{2(1 + c^2)^{3/2}} \frac{\bar{u}^2}{(u')^2} \bar{u}|u'|} \\ &= \overline{(1 + c^2)^{1/2} \bar{u}|u'|} + \overline{\frac{1}{(1 + c^2)^{1/2}} \bar{u}|u'|} + \overline{\frac{c^2}{2(1 + c^2)^{3/2}} \frac{\bar{u}^3}{|u'|}}. \end{aligned} \quad (\text{B9})$$

Once again assuming that c^2 is independent of longitude, the drag stress is then given by,

$$\overline{\tau_\phi} = c_D \rho_o \overline{(\bar{u} + u')|\bar{u} + u'|} \sim 2c_D \left(\overline{KE} \overline{KE'} \right)^{1/2} \left(\frac{2 + c^2}{(1 + c^2)^{1/2}} + \frac{c^2}{2(1 + c^2)^{3/2}} \frac{\overline{KE}}{\overline{KE'}} \right) \text{sgn}(\bar{u}), \quad (\text{B10})$$

or, if we neglect the stress due to meridional turbulence by assuming $c \ll 1$, then,

$$\overline{\tau_\phi} \sim 4c_D \left(\overline{KE} \overline{KE'} \right)^{1/2} \text{sgn}(\bar{u}). \quad (\text{B11})$$

Now the drag stress depends on the square root of the product of the zonal-mean zonal and turbulent kinetic energy densities, rather than their sum. In this case, no drag can be exerted if there is no turbulence, a consequence of the assumption $|u'| > |\bar{u}|$.

Acknowledgments

We thank two anonymous reviewers for their time and suggestions, which have improved the quality of this manuscript. Francis Nimmo for comments on an early draft of the manuscript, and Krista Soderlund, Yohai Kaspi, and Wanying Kang for fruitful discussions on rotating convection. H.H. thanks Jessie Brown, Divya Persaud, Erin Leonard, Samuel Howell, and Elodie Lesage for their discussions and encouragement. We are grateful to Jean-Michel Campin for providing the model configuration for our early numerical experiments. This work was supported by the National Aeronautics and Space Administration (NASA) through the Europa Clipper project. The research was carried out at the Jet Propulsion Laboratory, California Institute of Technology, under contract with NASA.

Data Availability Statement

A python notebook and all data files required to reproduce all figures in the manuscript can be found in the Zenodo repository at Hay (2023). The modified version of the MITgcm used to generate all numerical data is stored in the Zenodo repository at Campin et al. (2023).

References

- Amit, H., Choblet, G., Tobie, G., Terra-Nova, F., Čadež, O., & Bouffard, M. (2020). Cooling patterns in rotating thin spherical shells—Application to Titan's subsurface ocean. *Icarus*, 338, 113509. <https://doi.org/10.1016/j.icarus.2019.113509>
- Arya, S. P. S. (1975). A drag partition theory for determining the large-scale roughness parameter and wind stress on the Arctic pack ice. *Journal of Geophysical Research*, 80(24), 3447–3454. <https://doi.org/10.1029/JC080i024p03447>
- Ashkenazy, Y., & Tziperman, E. (2021). Dynamic Europa Ocean shows transient Taylor columns and convection driven by ice melting and salinity. *Nature Communications*, 12(1), 6376. <https://doi.org/10.1038/s41467-021-26710-0>
- Aurnou, J., Heimpel, M., & Wicht, J. (2007). The effects of vigorous mixing in a convective model of zonal flow on the ice giants. *Icarus*, 190(1), 110–126. <https://doi.org/10.1016/j.icarus.2007.02.024>
- Baland, R.-M., & Van Hoolst, T. (2010). Librations of the Galilean satellites: The influence of global internal liquid layers. *Icarus*, 209(2), 651–664. <https://doi.org/10.1016/j.icarus.2010.04.004>

- Barnes, R. T. H., Hide, R., White, A. A., & Wilson, C. A. (1983). Atmospheric angular momentum fluctuations, length-of-day changes and polar motion. *Proceedings of the Royal Society of London. A. Mathematical and Physical Sciences*, 387, 31–73. <https://doi.org/10.1098/rspa.1983.0050>
- Běhouňková, M., Tobie, G., Choblet, G., Kervazo, M., Melwani Daswani, M., Dumoulin, C., & Vance, S. D. (2021). Tidally induced magmatic pulses on the oceanic floor of Jupiter's Moon Europa. *Geophysical Research Letters*, 48(3), 1–11. <https://doi.org/10.1029/2020GL090077>
- Beuthe, M. (2016). Crustal control of dissipative ocean tides in Enceladus and other icy moons. *Icarus*, 280, 278–299. <https://doi.org/10.1016/j.icarus.2016.08.009>
- Bills, B. G., Nimmo, F., Karatekin, Ö., Van Hoolst, T., Rambaux, N., Levrard, B., & Laskar, J. (2009). Rotational dynamics of Europa. In *Europa* (pp. 119–134).
- Bills, B. G., & Scott, B. R. (2022). Rotation models for the Galilean satellites. *Planetary and Space Science*, 219, 105474. <https://doi.org/10.1016/j.pss.2022.105474>
- Bire, S., Kang, W., Ramadhan, A., Campin, J.-M., & Marshall, J. (2022). Exploring ocean circulation on icy Moons heated from below. *Journal of Geophysical Research: Planets*, 127(3), e2021JE007025. <https://doi.org/10.1029/2021JE007025>
- Böning, V. G. A., Wulff, P., Dietrich, W., Wicht, J., & Christensen, U. R. (2023). Direct driving of simulated planetary jets by upscale energy transfer. *Astronomy & Astrophysics*, 670, A15. <https://doi.org/10.1051/0004-6361/202244278>
- Busse, F. H. (2002). Convective flows in rapidly rotating spheres and their dynamo action. *Physics of Fluids*, 14(4), 1301–1314. <https://doi.org/10.1063/1.1455626>
- Campin, J.-M., Adcroft, A., Hill, C., & Marshall, J. (2004). Conservation of properties in a free-surface model. *Ocean Modelling*, 6(3), 221–244. [https://doi.org/10.1016/S1463-5003\(03\)00009-X](https://doi.org/10.1016/S1463-5003(03)00009-X)
- Campin, J.-M., Heimbach, P., Losch, M., Forget, G., edhill3, Adcroft, A., et al. (2023). hamishhay/mitgcm: Topdrag [Software]. Zenodo. <https://doi.org/10.5281/zenodo.7632806>
- Chao, B. F. (1989). Length-of-day variations caused by El Niño-Southern Oscillation and Quasi-Biennial Oscillation. *Science*, 243(4893), 923–925. <https://doi.org/10.1126/science.243.4893.923>
- Chen, E. M. A., & Nimmo, F. (2011). Obliquity tides do not significantly heat Enceladus. *Icarus*, 214(2), 779–781. <https://doi.org/10.1016/j.icarus.2011.06.007>
- Chen, E. M. A., Nimmo, F., & Glatzmaier, G. A. (2014). Tidal heating in icy satellite oceans. *Icarus*, 229, 11–30. <https://doi.org/10.1016/j.icarus.2013.10.024>
- Cheng, J. S., Aurnou, J. M., Julien, K., & Kunnen, R. P. (2018). A heuristic framework for next-generation models of geostrophic convective turbulence. *Geophysical & Astrophysical Fluid Dynamics*, 112(4), 277–300. <https://doi.org/10.1080/03091929.2018.1506024>
- Christensen, U. R. (2002). Zonal flow driven by strongly supercritical convection in rotating spherical shells. *Journal of Fluid Mechanics*, 470, 115–133. <https://doi.org/10.1017/S0022112002002008>
- Crawford, Z. A., & Pappalardo, R. T. (2006). Evidence for episodic formation of Europa's global lineaments via non-synchronous rotation. In *37th annual lunar and planetary science conference* (p. 2264).
- Deremble, B., Hogg, A. M., Berloff, P., & Dewar, W. (2011). On the application of no-slip lateral boundary conditions to “coarsely” resolved ocean models. *Ocean Modelling*, 39(3–4), 411–415. <https://doi.org/10.1016/j.ocemod.2011.05.002>
- Downey, B. G., Nimmo, F., & Matsuyama, I. (2020). Inclination damping on Callisto. *Monthly Notices of the Royal Astronomical Society*, 499(1), 40–51. <https://doi.org/10.1093/mnras/staa2802>
- Egbert, G. D., & Ray, R. D. (2001). Estimates of M_2 tidal energy dissipation from TOPEX/Poseidon altimeter data. *Journal of Geophysical Research: Oceans*, 106(C10), 22475–22502. <https://doi.org/10.1029/2000jc000699>
- Gastine, T., Wicht, J., & Aubert, J. (2016). Scaling regimes in spherical shell rotating convection. *Journal of Fluid Mechanics*, 808, 690–732. <https://doi.org/10.1017/jfm.2016.659>
- Gastine, T., Wicht, J., & Aurnou, J. M. (2015). Turbulent Rayleigh-Bénard convection in spherical shells. *Journal of Fluid Mechanics*, 778, 721–764. <https://doi.org/10.1017/jfm.2015.401>
- Geissler, P. E., Greenberg, R., Hoppa, G. V., Helfenstein, P., McEwen, A. S., Pappalardo, R. T., et al. (1998). Evidence for non-synchronous rotation of Europa. Galileo imaging team. *Nature*, 391(6665), 368–370. <https://doi.org/10.1038/34869>
- Gissinger, C., & Petitdemange, L. (2019). A magnetically driven equatorial jet in Europa's ocean. *Nature Astronomy*, 3(5), 401–407. <https://doi.org/10.1038/s41550-019-0713-3>
- Goldreich, P. M., & Mitchell, J. L. (2010). Elastic ice shells of synchronous moons: Implications for cracks on Europa and non-synchronous rotation of Titan. *Icarus*, 209(2), 631–638. <https://doi.org/10.1016/j.icarus.2010.04.013>
- Goodman, J. C., Collins, G. C., Marshall, J., & Pierrehumbert, R. T. (2004). Hydrothermal plume dynamics on Europa: Implications for chaos formation. *Journal of Geophysical Research: Planets*, 109(3), 1–19. <https://doi.org/10.1029/2003je002073>
- Goodman, J. C., & Lenferink, E. (2012). Numerical simulations of marine hydrothermal plumes for Europa and other icy worlds. *Icarus*, 221(2), 970–983. <https://doi.org/10.1016/j.icarus.2012.08.027>
- Goosse, H., & Fichet, T. (1999). Importance of ice-ocean interactions for the global ocean circulation: A model study. *Journal of Geophysical Research*, 104(C10), 23337–23355. <https://doi.org/10.1029/1999jc900215>
- Greenberg, R., & Weidenschilling, S. J. (1984). How fast do Galilean satellites spin? *Icarus*, 58(2), 186–196. [https://doi.org/10.1016/0019-1035\(84\)90038-1](https://doi.org/10.1016/0019-1035(84)90038-1)
- Hay, H. C. (2023). Supporting data for “turbulent drag at the ice-ocean interface of Europa in simulations of rotating convection: Implications for nonsynchronous rotation of the ice shell” [Dataset]. Zenodo. <https://doi.org/10.5281/zenodo.7632248>
- Hay, H. C., & Matsuyama, I. (2017). Numerically modelling tidal dissipation with bottom drag in the oceans of Titan and Enceladus. *Icarus*, 281, 342–356. <https://doi.org/10.1016/j.icarus.2016.09.022>
- Hay, H. C., & Matsuyama, I. (2019). Nonlinear tidal dissipation in the subsurface oceans of Enceladus and other icy satellites. *Icarus*, 319, 68–85. <https://doi.org/10.1016/j.icarus.2018.09.019>
- Hay, H. C., Matsuyama, I., & Pappalardo, R. T. (2022). The high-frequency tidal response of ocean worlds: Application to Europa and Ganymede. *Journal of Geophysical Research: Planets*, 127(5). <https://doi.org/10.1029/2021JE007064>
- Hay, H. C., Trinh, A., & Matsuyama, I. (2020). Powering the Galilean satellites with Moon-Moon tides. *Geophysical Research Letters*, 47(15), e2020GL088317. <https://doi.org/10.1029/2020GL088317>
- Heimpel, M., & Aurnou, J. (2007). Turbulent convection in rapidly rotating spherical shells: A model for equatorial and high latitude jets on Jupiter and Saturn. *Icarus*, 187(2), 540–557. <https://doi.org/10.1016/j.icarus.2006.10.023>
- Hoppa, G., Greenberg, R., Geissler, P., Tufts, B. R., Plassmann, J., & Durda, D. D. (1999). Rotation of Europa: Constraints from terminator and limb positions. *Icarus*, 137(2), 341–347. <https://doi.org/10.1006/icar.1998.6065>
- Howell, S. M. (2021). The likely thickness of Europa's icy shell. *The Planetary Science Journal*, 2(4), 129. <https://doi.org/10.3847/PSJ/abfe10>

- Hurford, T. A., Sarid, A. R., & Greenberg, R. (2007). Cycloidal cracks on Europa: Improved modeling and non-synchronous rotation implications. *Icarus*, 186(1), 218–233. <https://doi.org/10.1016/j.icarus.2006.08.026>
- Husmann, H., & Spohn, T. (2004). Thermal-orbital evolution of Io and Europa. *Icarus*, 171(2), 391–410. <https://doi.org/10.1016/j.icarus.2004.05.020>
- Jansen, M. F., Kang, W., & Kite, E. (2022). Energetics govern ocean circulation on icy ocean worlds. arXiv:2206.00732. arXiv. <https://doi.org/10.48550/arXiv.2206.00732>
- Jara-Orué, H. M., & Vermeersen, B. L. (2011). Effects of low-viscous layers and a non-zero obliquity on surface stresses induced by diurnal tides and non-synchronous rotation: The case of Europa. *Icarus*, 215(1), 417–438. <https://doi.org/10.1016/j.icarus.2011.05.034>
- Jayne, S. R., & St. Laurent, L. C. (2001). Parameterizing tidal dissipation over rough topography. *Geophysical Research Letters*, 28(5), 811–814. <https://doi.org/10.1029/2000GL012044>
- Kaspi, Y., Flierl, G. R., & Showman, A. P. (2009). The deep wind structure of the giant planets: Results from an anelastic general circulation model. *Icarus*, 202(2), 525–542. <https://doi.org/10.1016/j.icarus.2009.03.026>
- Kattenhorn, S. A. (2002). Nonsynchronous rotation evidence and fracture history in the bright plains region, Europa. *Icarus*, 157(2), 490–506. <https://doi.org/10.1006/icar.2002.6825>
- King, E. M., Stellmach, S., Noir, J., Hansen, U., & Aurnou, J. M. (2009). Boundary layer control of rotating convection systems. *Nature*, 457(7227), 301–304. <https://doi.org/10.1038/nature07647>
- Kworka, J., & Čadež, O. (2022). A numerical model of convective heat transfer in Titan's subsurface ocean. *Icarus*, 376, 114853. <https://doi.org/10.1016/j.icarus.2021.114853>
- Lambeck, K. (1980). *The Earth's variable rotation: Geophysical causes and consequences*. Cambridge University Press.
- Lewis, E. L., & Perkin, R. G. (1986). Ice pumps and their rates. *Journal of Geophysical Research*, 91(C10), 11756–11762. <https://doi.org/10.1029/JC091iC10p11756>
- Lobo, A. H., Thompson, A. F., Vance, S. D., & Tharimena, S. (2021). A pole-to-equator ocean overturning circulation on Enceladus. *Nature Geoscience*, 14(4), 185–189. <https://doi.org/10.1038/s41561-021-00706-3>
- Lu, P., Li, Z., Cheng, B., & Leppäranta, M. (2011). A parameterization of the ice-ocean drag coefficient. *Journal of Geophysical Research*, 116(7), 1–14. <https://doi.org/10.1029/2010JC006878>
- Madden, R. A., & Speth, P. (1995). Estimates of atmospheric angular momentum, friction, and mountain torques during 1987–1988. *Journal of the Atmospheric Sciences*, 52(21), 3681–3694. [https://doi.org/10.1175/1520-0469\(1995\)052<3681:EOAAMF>2.0.CO;2](https://doi.org/10.1175/1520-0469(1995)052<3681:EOAAMF>2.0.CO;2)
- Marshall, J., Adcroft, A., Hill, C., Perelman, L., & Heisey, C. (1997). A finite-volume, incompressible Navier Stokes model for studies of the ocean on parallel computers. *Journal of Geophysical Research*, 102(C3), 5753–5766. <https://doi.org/10.1029/96JC02775>
- Matsuyama, I., Beuthe, M., Hay, H. C. F. C., Nimmo, F., & Kamata, S. (2018). Ocean tidal heating in icy satellites with solid shells. *Icarus*, 312, 208–230. <https://doi.org/10.1016/j.icarus.2018.04.013>
- McEwen, A. S. (1986). Tidal reorientation and the fracturing of Jupiter's Moon Europa. *Nature*, 321(6065), 49–51. <https://doi.org/10.1038/321049a0>
- Miquel, B., Xie, J. H., Featherstone, N., Julien, K., & Knobloch, E. (2018). Equatorially trapped convection in a rapidly rotating shallow shell. *Physical Review Fluids*, 3(5), 053801. <https://doi.org/10.1103/PhysRevFluids.3.053801>
- Munk, W., & Groves, G. (1952). The effect of winds and ocean currents on the annual variation in latitude. *Journal of the Atmospheric Sciences*, 9(6), 385–396. [https://doi.org/10.1175/1520-0469\(1952\)009<0385:TEOWAO>2.0.CO;2](https://doi.org/10.1175/1520-0469(1952)009<0385:TEOWAO>2.0.CO;2)
- Munk, W., & MacDonald, G. J. F. (1960). The rotation of the Earth a geophysical discussion.
- Nimmo, F. (2004). Non-Newtonian topographic relaxation on Europa. *Icarus*, 168(1), 205–208. <https://doi.org/10.1016/j.icarus.2003.11.022>
- O'Brien, D. P., Geissler, P., & Greenberg, R. (2002). A melt-through model for chaos formation on Europa. *Icarus*, 156(1), 152–161. <https://doi.org/10.1006/icar.2001.6777>
- Ojakangas, G. W., & Stevenson, D. J. (1989). Thermal state of an ice shell on Europa. *Icarus*, 241(2), 220–241. [https://doi.org/10.1016/0019-1035\(89\)90052-3](https://doi.org/10.1016/0019-1035(89)90052-3)
- Pathhoff, D. A., Kattenhorn, S. A., & Cooper, C. M. (2019). Implications of nonsynchronous rotation on the deformational history and ice shell properties in the south polar terrain of Enceladus. *Icarus*, 321, 445–457. <https://doi.org/10.1016/j.icarus.2018.11.028>
- Rambaux, N., Van Hoolst, T., & Karatekin, Ö. (2011). Librational response of Europa, Ganymede, and Callisto with an ocean for a non-Keplerian orbit. *Astronomy and Astrophysics*, 527(15), A118. <https://doi.org/10.1051/0004-6361/201015304>
- Rhoden, A. R., Burkhard, M., Huff, E. M., Hurford, T. A., Manga, M., & Richards, M. A. (2010). Constraints on Europa's rotational dynamics from modeling of tidally-driven fractures. *Icarus*, 210(2), 770–784. <https://doi.org/10.1016/j.icarus.2010.07.018>
- Rhoden, A. R., & Hurford, T. A. (2013). Lineament azimuths on Europa: Implications for obliquity and non-synchronous rotation. *Icarus*, 226(1), 841–859. <https://doi.org/10.1016/j.icarus.2013.06.029>
- Ronchi, C., Iacono, R., & Paolucci, P. (1996). The “cubed sphere”: A new method for the solution of partial differential equations in spherical geometry. *Journal of Computational Physics*, 124(1), 93–114. <https://doi.org/10.1006/jcph.1996.0047>
- Rosen, R. D., & Salstein, D. A. (1983). Variations in atmospheric angular momentum on global and regional scales and the length of day. *Journal of Geophysical Research*, 88(C9), 5451–5470. <https://doi.org/10.1029/JC088iC09p05451>
- Rovira-Navarro, M., Gerkema, T., Maas, L. R., van der Wal, W., van Ostayen, R., & Vermeersen, B. (2020). Tides in subsurface oceans with meridional varying thickness. *Icarus*, 343, 113711. <https://doi.org/10.1016/j.icarus.2020.113711>
- Selvans, Z. A. (2009). *Time, tides, and tectonics on icy satellites*. Doctoral dissertation. <https://doi.org/10.5281/zenodo.3455893>
- Shirasawa, K. (1986). Water stress and ocean current measurements under first-year sea ice in the Canadian Arctic. *Journal of Geophysical Research*, 91(C12), 14305–14316. <https://doi.org/10.1029/JC091iC12p14305>
- Shirasawa, K., & Ingram, R. G. (1991). Characteristics of the turbulent oceanic boundary layer under sea ice. Part 1: A review of the ice-ocean boundary layer. *Journal of Marine Systems*, 2(1), 153–160. [https://doi.org/10.1016/0924-7963\(91\)90021-L](https://doi.org/10.1016/0924-7963(91)90021-L)
- Showman, A. P., Kaspi, Y., & Flierl, G. R. (2011). Scaling laws for convection and jet speeds in the giant planets. *Icarus*, 211(2), 1258–1273. <https://doi.org/10.1016/j.icarus.2010.11.004>
- Soderlund, K. M. (2019). Ocean dynamics of outer solar system satellites. *Geophysical Research Letters*, 46(15), 8700–8710. <https://doi.org/10.1029/2018GL081880>
- Soderlund, K. M., Heimpel, M. H., King, E. M., & Aurnou, J. M. (2013). Turbulent models of ice giant internal dynamics: Dynamos, heat transfer, and zonal flows. *Icarus*, 224(1), 97–113. <https://doi.org/10.1016/j.icarus.2013.02.014>
- Soderlund, K. M., Schmidt, B. E., Wicht, J., & Blankenship, D. D. (2014). Ocean-driven heating of Europa's icy shell at low latitudes. *Nature Geoscience*, 7(1), 16–19. <https://doi.org/10.1038/ngeo2021>
- Spaun, N. A. (2002). *Chaos, lenticulae, and lineae on Europa: Implications for geological history, crustal thickness, and the presence of an ocean*. Doctoral dissertation, Brown University. Retrieved from <https://www.proquest.com/dissertations-theses/chaos-lenticulae-lineae-on-europa-implications/docview/304783845/se-2>

- Steele, M., Morison, J. H., & Unterstener, N. (1989). The partition of air-ice-ocean momentum exchange as a function of ice concentration, floe size, and draft. *Journal of Geophysical Research*, 94(C9), 12739. <https://doi.org/10.1029/jc094ic09p12739>
- Tyler, R. (2008). Strong ocean tidal flow and heating on moons of the outer planets. *Nature*, 456(7223), 770–772. <https://doi.org/10.1038/nature07571>
- Tyler, R. (2011). Tidal dynamical considerations constrain the state of an ocean on Enceladus. *Icarus*, 211(1), 770–779. <https://doi.org/10.1016/j.icarus.2010.10.007>
- Van Hoolst, T., Rambaux, N., Karatekin, Ö., Dehant, V., & Rivoldini, A. (2008). The librations, shape, and icy shell of Europa. *Icarus*, 195(1), 386–399. <https://doi.org/10.1016/j.icarus.2007.12.011>
- Vincent, D., Lambrechts, J., Tyler, R. H., Karatekin, Ö., Dehant, V., & Deleersnijder, É. (2022). A numerical study of the liquid motion in Titan's subsurface ocean. *Icarus*, 388, 115219. <https://doi.org/10.1016/j.icarus.2022.115219>
- Von Karman, T. H. (1931). Mechanical similitude and turbulence.
- Wahr, J. M. (1983). The effects of the atmosphere and oceans on the Earth's wobble and on the seasonal variations in the length of day—II. Results. *Geophysical Journal International*, 74(2), 451–487. <https://doi.org/10.1111/j.1365-246X.1983.tb01885.x>
- Wahr, J. M., Sasao, T., & Smith, M. L. (1981). Effect of the fluid core on changes in the length of day due to long period tides. *Geophysical Journal of the Royal Astronomical Society*, 64(3), 635–650. <https://doi.org/10.1111/j.1365-246X.1981.tb02688.x>
- Wahr, J. M., Zuber, M. T., Smith, D. E., & Lunine, J. I. (2006). Tides on Europa, and the thickness of Europa's icy shell. *Journal of Geophysical Research: Planets*, 111(12), 1–10. <https://doi.org/10.1029/2006JE002729>
- Yoder, C. F. (1979). How tidal heating in Io drives the Galilean orbital resonance locks. *Nature*, 279(5716), 767–770. <https://doi.org/10.1038/279767a0>
- Zahnle, K., Alvarellos, J. L., Dobrovolskis, A., & Hamill, P. (2008). Secondary and sesquinary craters on Europa. *Icarus*, 194(2), 660–674. <https://doi.org/10.1016/j.icarus.2007.10.024>
- Zahnle, K., Dones, L., & Levison, H. F. (1998). Cratering rates on the Galilean satellites. *Icarus*, 136(2), 202–222. <https://doi.org/10.1006/icar.1998.6015>
- Zahnle, K., Schenk, P., Levison, H., & Dones, L. (2003). Cratering rates in the outer solar system. *Icarus*, 163(2), 263–289. [https://doi.org/10.1016/S0019-1035\(03\)00048-4](https://doi.org/10.1016/S0019-1035(03)00048-4)
- Zahnle, K., Schenk, P., Sobieszczyk, S., Dones, L., & Levison, H. F. (2001). Differential cratering of synchronously rotating satellites by ecliptic comets. *Icarus*, 153(1), 111–129. <https://doi.org/10.1006/icar.2001.6668>
- Zeng, Y., & Jansen, M. F. (2021). Ocean circulation on Enceladus with a high-versus low-salinity Ocean. *Planetary Science Journal*, 2(4), 151. <https://doi.org/10.3847/PSJ/ac1114>
- Zhu, P., Manucharyan, G. E., Thompson, A. F., Goodman, J. C., & Vance, S. D. (2017). The influence of meridional ice transport on Europa's ocean stratification and heat content. *Geophysical Research Letters*, 44(12), 5969–5977. <https://doi.org/10.1002/2017GL072996>
- Zimmer, C., Khurana, K. K., & Kivelson, M. G. (2000). Subsurface oceans on Europa and Callisto: Constraints from Galileo magnetometer observations. *Icarus*, 147(2), 329–347. <https://doi.org/10.1006/icar.2000.6456>

References From the Supporting Information

Vallis, G. K. (2017). *Atmospheric and oceanic fluid dynamics*. Cambridge University Press.

Erratum

In the originally published version of this article, the following sentence was omitted from the Acknowledgments: “We are grateful to Jean-Michel Campin for providing the model configuration for our early numerical experiments.” In addition, the citations “Rhoden et al., (2010)” and “Rhoden & Hurford (2013)” were omitted from the eighth sentence of the third paragraph of the Introduction. The sentence should read: “Yet, a large number of tectonic features on the surface can be explained most easily by the presence of nonsynchronous rotation (Geissler et al., 1998; Hurford et al., 2007; Jara-Orué & Vermeersen, 2011; Kattenhorn, 2002; McEwen, 1986; Rhoden & Hurford, 2013; Rhoden et al., 2010; Selvans, 2009; Spaun, 2002) and have also been suggested for Enceladus (Pathhoff et al., 2019).” The full references have been added to the reference section. All errors have been corrected, and this version may be considered the authoritative version of record.